

1
2 **Organic matter sulfurization and organic carbon burial in the Mesoproterozoic**
3

4 Morgan Reed Raven,^{a*} Peter W. Crockford,^b Malcolm S. W. Hodgskiss,^c Timothy W. Lyons,^d
5 Christopher J. Tino,^d Samuel M. Webb^e
6

7 ^a Dept. of Earth Science, University of California Santa Barbara, Santa Barbara, CA 93106 USA

8 ^b Woods Hole Oceanographic Institution, Woods Hole MA 02543 USA

9 ^c Geological Survey of Norway, Trondheim 7040, Norway

10 ^d Department of Earth and Planetary Sciences, University of California Riverside, Riverside, CA 92521
11 USA

12 ^e Stanford Synchrotron Radiation Lightsource, SLAC National Accelerator Lab, Menlo Park CA, 94025
13 USA

14 * corresponding author: *raven@ucsb.edu*
15
16

17 **Abstract**

18 Throughout the Proterozoic Era, sedimentary organic carbon burial helped set the pace of global
19 oxygenation and acted as a major modulator of atmospheric CO₂ and climate. Although Proterozoic rocks
20 generally contain low concentrations of organic matter (OM), there are key exceptions to this rule, including
21 the relatively OM-rich Arctic Bay shales from Baffin Island, Canada (Bylot Supergroup, Borden Basin,
22 ~1.05 Ga). The mechanisms driving elevated OM concentrations in these and other Proterozoic shales
23 remain poorly understood. In the Mesozoic and Cenozoic, organic matter sulfurization can be a major driver
24 of enhanced OM burial across a range of redox conditions comparable to those inferred for many
25 Proterozoic environments. Therefore, in this study, we evaluate the role of sulfurization in driving OM
26 preservation in the Mesoproterozoic Borden Basin and discuss its relevance to Proterozoic systems in
27 general. We present the first evidence for syngenetic-to-early-diagenetic OM sulfurization in a Proterozoic
28 basin, which begins to fill a several-billion-year gap in our record of organic S across Earth history. We
29 find that OM sulfurization was particularly extensive in shales from a relatively shallow-water section
30 (Alpha River) but less extensive in shales deposited in deeper water (Shale Valley), which is consistent
31 with models that infer sulfidic ‘wedges’ or O₂-minimum-zone-type structures on shelf margins at least
32 intermittently at this time. At the shallower site, organic S and pyrite are similarly ³⁴S-depleted and thus
33 likely formed at roughly the same time near the sediment-water interface under conditions previously
34 interpreted to have been ferruginous to intermittently sulfidic. In contrast, at the deeper-water site, large S-
35 isotope differences between pyrite and organic S along with low apparent OM sulfurization intensities
36 indicate that pyrite formation was favored over OM sulfurization during early sedimentation under variable
37 but primarily ferruginous conditions. Although Mesoproterozoic biomass can be substantially sulfurized,
38 indicators of sulfurization intensity are not correlated with OM concentrations, and therefore sulfurization
39 does not appear to have been the primary driver of enhanced OM concentrations in Arctic Bay Formation

40 shales. The link between sulfurization and total OM preservation may have been modulated during the
41 deposition of Arctic Bay Formation shales by differences in iron availability, nutrient cycling, and particle
42 dynamics in the Mesoproterozoic.
43

1. INTRODUCTION

Organic carbon burial in marine sediments is a fundamental control on the biogeochemical evolution of Earth, particularly surface environment oxygenation. Integrated across the Proterozoic, the mechanisms influencing rates of organic carbon burial were crucial factors impacting both the size of the surface reservoir of O₂ and the concentration of CO₂ in the atmosphere. Although Proterozoic rocks generally contain low concentrations of total organic carbon (TOC) (Sperling and Stockey, 2018; Woltz et al., 2021), the TOC-rich shales of the Arctic Bay Formation from Baffin Island, Canada, are a notable exception (Kah et al., 2001; Hahn and Turner, 2017). A 100-meter-thick section of the Arctic Bay Formation at Alpha River, for example, contains an average of 4.8 wt% TOC (n=22, range 0.74 to 12.3 wt%) (Hodgskiss et al., 2020). The mechanisms that support enhanced organic carbon burial in deposits like these shales thus have the potential to influence the global balances of carbon and oxygen throughout the Proterozoic.

Organic carbon burial fluxes depend on both rates of local primary productivity and the efficiency of organic matter (OM) preservation in the environment. Primary productivity was generally low and predominantly cyanobacterial in the Mesoproterozoic (Derry, 2015; Crockford et al., 2018; Duda et al., 2021), although local, riverine or upwelling-derived inputs of phosphate may have supported higher productivity near river mouths or other ocean margin settings (Laakso and Schrag, 2019). Some proportion of this primary productivity was delivered to, and buried in, sediments, through a variety of preservation mechanisms. High organic carbon burial efficiencies (defined here as the proportion of OM exported from the surface ocean that was preserved in underlying sediment) have been proposed to help balance the global carbon cycle across long intervals of Earth history when rates of primary productivity are inferred to have been significantly lower than today (Kipp et al., 2021). Despite their potential importance for Earth's redox evolution, however, the specific mechanisms that may have led to high organic carbon burial efficiency in the Proterozoic remain largely untested.

The likelihood of OM being preserved over geologic timescales in sediments depends first upon its delivery to sediments for burial, for example within sinking particles. The susceptibility of OM to remineralization by microbial heterotrophs in both particles and sediments can be reduced if OM is associated with mineral surfaces (Hemingway et al., 2019) or chemically transformed into less functionalized, higher-molecular-weight, polymeric materials. Another factor impacting OM burial efficiency is O₂ exposure time (Hartnett et al., 1998), which reflects the redox structure of the local environment. Longer O₂ exposure times and oxic conditions are associated with low burial efficiencies due to thorough breakdown and remineralization by aerobic micro- and macroscopic organisms. Alternatively, anoxic conditions – whether they result from

78 high export productivity, high sedimentation rates, circulation patterns, or other factors – enhance OM
79 preservation efficiency in part because organisms gain less energy from anaerobic metabolisms and grow
80 more slowly (Canfield, 1994; Jin and Bethke, 2005). Although it has not been widely explored in
81 Precambrian systems, anoxic conditions also have the potential to enhance OM preservation through OM
82 sulfurization.

83

84 Sulfurization can occur in anoxic and sulfidic settings, in either the sediments or the water column.
85 Dissolved sulfide (mostly HS⁻) and polysulfides (S_x²⁻) sulfurize organic matter through reactions with
86 certain reactive functional groups that are common in carbohydrates and lipids, including aldehydes and
87 conjugated double bonds (Sinninghe Damsté and de Leeuw, 1990; Kohnen et al., 1991). These reactions
88 increase the S:C ratio of OM beyond that of microbial biomass (0.5–2 mol%, where 1 mol% is defined as
89 S:C = 1:100 mol/mol or a molar ratio of 0.01; Matrai and Eppley, 1989; Chen et al., 1996) and yield
90 polymeric materials that are more likely than their precursors to be preserved over long timescales in
91 sediments and rocks, thereby enhancing OM burial. Accordingly, higher OM S:C ratios are frequently
92 associated with higher OM concentrations in shales (Boussafir et al., 1995; Van Kaam-Peters et al., 1998),
93 with Ocean Anoxic Event 2 in the Cretaceous (94 Mya) serving as a prominent example of this phenomenon
94 (Raven et al., 2019). Modern sites with substantially sulfurized OM (S:C > ~2 mol%) also typically produce
95 sediments with elevated OM concentrations (TOC > 3 wt%). Such environments include intermittently
96 anoxic to sulfidic basins (Werne et al., 2003; Raven et al., 2016) and the anoxic regions of upwelling zones
97 along the Namibian and Peruvian margins (Eglinton et al., 1994; Dale et al., 2009). Although sulfurization
98 reactions affect organic materials, they are abiotic and have the potential to operate similarly at any point
99 in Earth history if sulfurizable precursors are present. Therefore, elevated OM concentrations in
100 Mesoproterozoic shales could, by analogy to Phanerozoic trends, reflect extensive sulfurization. At the same
101 time, sulfurization is just one of several potential mechanisms for OM preservation in shales; for example,
102 substantial amounts of OM can also be protected against microbial degradation by rapid burial and
103 association with clays and other mineral surfaces (Suess, 1973; Ingall and Cappellen, 1990; Hedges and
104 Keil, 1995; Kennedy et al., 2014). Given differences in the redox structure, productivity, and biomass
105 characteristics of Mesoproterozoic basins, the mechanisms driving locally elevated OM concentrations at
106 that time remain an outstanding problem in the Proterozoic.

107

108 Organic sulfurization products can be distinguished from biogenic organic S by their S-isotope composition
109 as well as their redox speciation. Biogenic S is predominantly assimilated from seawater sulfate and
110 approximately matches its S-isotope composition (Trust and Fry, 1992). Seawater sulfate concentrations in
111 the Mesoproterozoic were likely a few millimolar (1.5 – 4.5 mM) (Kah et al., 2004) although estimates

112 range from a few hundred micromolar (Fakraee et al., 2019) to as high as 6–10 mM (Blättler et al., 2020),
113 compared with 28 mM today. The S-isotope composition of Mesoproterozoic seawater sulfate has been
114 estimated from carbonate-associated sulfate as well as nodular and bedded evaporites (gypsum; CaSO₄)
115 from within the same basin as the Arctic Bay Formation, namely the overlying Iqqituq and Angmaat
116 formations (formerly part of the Society Cliffs Formation), which range from +21.5‰ to +36.4‰ (Kah et
117 al., 2001; Crockford et al., 2019). These data represent our best estimate for Mesoproterozoic seawater
118 sulfate and, by extension, phytoplankton biomass $\delta^{34}\text{S}$ values. In contrast, sulfide produced during
119 microbial sulfate reduction (MSR) has a distinctively ³⁴S-depleted composition, with $\delta^{34}\text{S}$ values that are
120 typically 15–70‰ lower than contemporaneous sulfate (Kaplan and Rittenberg, 1964; Sim et al., 2011).
121 This signal can subsequently be recorded in abiogenic organic sulfur with a relatively small (typically 4–
122 5‰) additional isotope fractionation (Amrani and Aizenshtat, 2004a; Amrani et al., 2008), although
123 substantial inter-compound variability is possible (Raven et al., 2015; Rosenberg et al., 2017; Shawar et al.,
124 2020). The S-isotope composition of sulfide-derived organic S thus generally resembles sulfide and other
125 sulfide-derived phases, most notably pyrite (FeS₂) (Vairavamurthy et al., 1995).

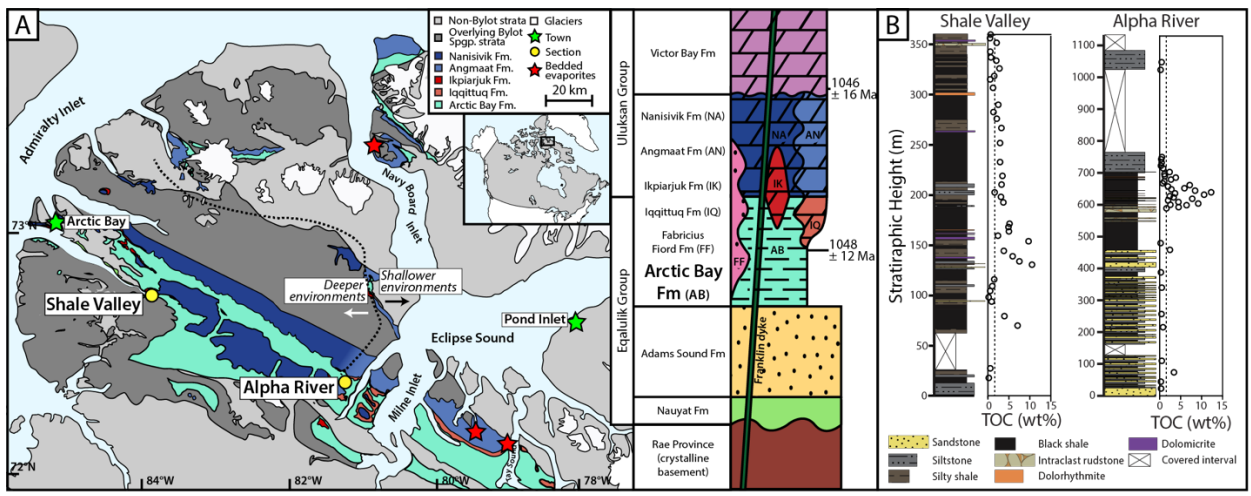
126
127 In the Mesoproterozoic, many shallow marine environments may have been favorable locations for OM
128 sulfurization. Atmospheric O₂ concentrations were likely ~0.1-10% of modern levels, and the deep ocean
129 was largely anoxic, with transient, localized sulfidic conditions on continental shelves (Lyons et al., 2014;
130 Planavsky et al., 2014, 2018; Cole et al., 2016; Stolper and Keller, 2018). Upwelling and weathering-
131 derived sources of nutrients to the continental shelves likely supported enhanced productivity in coastal
132 environments (Laakso and Schrag, 2019). Across the Proterozoic, the deep ocean is thought to have been
133 predominantly ferruginous, meaning that the Eh of the environment was buffered by the Fe³⁺/Fe²⁺ redox
134 couple (Poulton and Canfield, 2011; Planavsky et al., 2011) and that dissolved Fe²⁺ concentrations may
135 have been high (micromolar). Importantly, however, many redox reconstructions for this time period rely
136 on the iron speciation proxy, which is subject to depositional and diagenetic effects that can in certain cases
137 reduce confidence in its interpretation (Pasquier et al., 2022). There is also growing evidence that the deeper
138 portion of the Proterozoic water column may have been characterized by more dynamic redox conditions
139 than previously suggested, with intermittent oxygenation (Knoll and Sperling, 2014; Zhang et al., 2018;
140 Diamond and Lyons, 2018; Hodgskiss et al., 2020) or nitrogenous conditions, buffered instead by the
141 nitrate/nitrite redox couple (Michiels et al., 2017; Stüeken et al., 2021). The differences between different
142 possible ‘flavors’ of Proterozoic ocean anoxia – e.g, ferruginous versus nitrogenous versus sulfidic
143 conditions and the dynamic transitions among these end-members – are critically important for organic
144 carbon burial due to their impacts on both the favorability of various metabolic pathways and the activities
145 of different preservation mechanisms for sedimentary organic matter. In terms of the favorability of OM

146 sulfurization, sulfidic and potentially nitrogenous conditions may provide the conditions necessary to
 147 support early OM sulfurization in the water column or near the sediment-water interface. However, elevated
 148 concentrations of Fe^{2+} under ferruginous conditions have the potential to react rapidly with any available
 149 sulfide to produce iron sulfide solids (primarily FeS and FeS_2) and thus limit the sulfide available for OM
 150 sulfurization in the water column.

151
 152 Here, we present a detailed assessment of the S-isotope compositions and speciation of organic and
 153 inorganic sulfur phases in two stratigraphic sections from the late Mesoproterozoic Arctic Bay Formation,
 154 which have been interpreted to record a range of oxic, ferruginous, and intermittently sulfidic conditions
 155 (Hodgskiss et al., 2020). We use these data to evaluate the mechanisms that contributed to organic matter
 156 preservation in the mid-Proterozoic, testing the relationship between organic matter sulfurization and
 157 elevated organic carbon preservation in ancient, anoxic oceans. By comparing patterns in the S-isotope
 158 compositions of sulfate, pyrite, and organic sulfur, we evaluate the potential locations and pathways of
 159 pyrite and organic sulfur formation in the ancient environment and, by extension, its organic carbon cycle
 160 and redox structure.

161
 162
 163 **2. MATERIALS AND METHODS**

164
 165 **2.1 Geological Context**



167
 168 **Fig. 1 Site overview, stratigraphy and organic carbon content.** Modified from Hodgskiss et al., 2020
 169 figs. 1 and 5. Dotted line on panel 'A' shows the 'deeper' to 'shallower' facies transition as interpreted
 170 from the depositional facies of the overlying Angmaat/Iqittuq/Nanisivik formations (Turner and Kamber,

171 2012). Dashed vertical line in both panels in ‘B’ shows median late Mesoproterozoic TOC values (Sperling
172 and Stockey, 2018).

173

174 Samples for this study come from the Arctic Bay Formation, Bylot Supergroup, Borden Basin, northern
175 Baffin Island, Nunavut, Canada. Age control is provided by Re-Os dates of 1048 ± 12 Ma for the middle-
176 upper Arctic Bay Formation and 1046 ± 16 Ma for the overlying Victor Bay Formation (Gibson et al.,
177 2018). The Arctic Bay Formation is a thick section (180 – 1130 m, thinning to the northwest; Turner and
178 Kamber, 2012) of OM-rich shales; the lower interval contains repeating shale-silt-sand shallowing-upward
179 packages, and the upper interval contains interbedded black shales, silty shales and silts without regular
180 cyclicity. The Shale Valley section (“T1413”; N72.75133°, W83.84422°) spans 358 m from the lower
181 Arctic Bay to the overlying contact in the Ikpiarjuk Fm. The Alpha River site is a composite of two
182 shallower-water sections (“PWC1405” and “MB1401”; N72.39550°, W81.18947°) spanning 1130 m of
183 stratigraphy from underlying Adams Sound to overlying Iqqittuq Fm. Although both sites record
184 approximately the same time interval, Alpha River and Shale Valley records have not been directly
185 correlated because they are ~90 km apart, are affected by low-angle erosive hiatuses, and lack marker beds
186 (Turner and Kamber, 2012; Hodgskiss et al., 2020). Total carbon, nitrogen, and sulfur contents, bulk N and
187 organic C isotope data, trace element concentrations, and iron speciation for these sections were presented
188 in Hodgskiss et al. (2020).

189

190 The Arctic Bay Formation is underlain by the Adams Sound Formation, a thick (up to 610 m; Long and
191 Turner, 2012) quartz arenite representing shallow marine deposition. Active normal faulting in the basin is
192 thought to have led to rapid subsidence and deposition of Arctic Bay Formation shales, siltstones, and
193 sandstones along a gentle depth gradient, deepening to the present-day northwest (Turner and Kamber,
194 2012). The lower Arctic Bay Formation contains a series of shallowing-upward clastic cycles. In the Alpha
195 River section, which records relatively shallow-water deposition, black shales containing as much as 12.3
196 wt% TOC are concentrated in a roughly 100-m-thick interval in the middle of the formation; these are
197 overlain by layers of black shale and siltstone. The Shale Valley section reflects a deeper environment and
198 is composed of interbedded siltstones and black shales. TOC concentrations in Shale Valley are generally
199 higher in the lower part of the section (averaging 4.8 wt% from 0 – 170 m) and moderate in the upper part
200 (averaging 2.1 wt% from 170 – 351 m) (Hodgskiss et al., 2020). Following the deposition of the Arctic Bay
201 Formation, deposition in the shallower part of the basin is recorded in the Iqqittuq Formation, which
202 reflects a carbonate ramp environment and is composed of interbedded dolomicrite and shale. In the deeper
203 (northwest) part of the basin, the Arctic Bay Formation is overlain by the Ikpiarjuk Formation, consisting
204 of dolostone mounds that may reflect fluid venting along faults (Hahn and Turner, 2017). Carbonates

205 continued to dominate subsequent deposition in both regions. Units overlying the Arctic Bay Formation
206 were previously grouped together and called the ‘Society Cliffs Formation’ (Blackadar and Lemon, 1963).
207 The lower part of these carbonates also contains evaporitic facies, including laterally continuous massive
208 and laminated gypsum (CaSO_4) beds that appear to reflect precipitation in the water column in some
209 locations and small, decimeter-scale pods in other locations within the basin. This gypsum has $\delta^{34}\text{S}$ values
210 between +21.5 and 36.4‰ (Kah et al., 2004; Crockford et al., 2019).

211
212 The degree of connectivity between the Borden Basin and the global ocean is uncertain but likely varied
213 through time. The high availability of sulfate and some metals (Hodgskiss et al., 2020) argues for at least
214 an occasional marine connection (e.g., during deposition of the Iqqituuq and Angmaat formations overlying
215 the Arctic Bay Formation). However, based on initial Os isotope values and REE+Y trends, some authors
216 have argued that the Arctic Bay Formation was deposited in a much more restricted setting such as an
217 alkaline lacustrine environment (Hahn et al., 2015; Gibson et al., 2019).

218
219 The redox structure of the Arctic Bay depositional environment is constrained by iron speciation and trace
220 metal abundance records in the context of global Mesoproterozoic redox evolution. Based on elevated total
221 S contents and enrichments in Mo, U, and V (Hodgskiss et al., 2020), the lower half of the Shale Valley
222 section appears to have been ferruginous and intermittently euxinic. In the Alpha River section, the highest
223 TOC contents are found between 580-780 m of stratigraphic height. These shales are also characterized by
224 relatively high degree of pyritization, although ratios of pyrite iron (Fe_{py}) to highly reactive iron (Fe_{HR}) are
225 below canonical thresholds for euxinia (~0.6 versus ~0.7). These Alpha River black shales are particularly
226 notable for containing ‘excess’ sulfur beyond that attributable to barite or pyrite, which, if associated with
227 organic matter, would imply remarkably high kerogen S:C ratios (Hodgskiss et al., 2020). Other parts of
228 both sections, however, indicate primarily ferruginous (anoxic, non-sulfidic) conditions. Carbonate-
229 associated iron (Fe_{carb}) is abundant and can comprise up to half of the highly reactive iron pool (Fe_{HR})
230 (Hodgskiss et al., 2020).

231
232 Although global productivity during the Mesoproterozoic is thought to have been relatively low due to
233 nutrient limitation under anoxic deep ocean conditions (Derry, 2015; reviewed in Lyons et al., 2021),
234 productivity in the Borden Basin may have been locally high due to a riverine or other influx of phosphate
235 (Laakso and Schrag, 2019). High TOC contents in the Arctic Bay Formation persist despite ca. 1 Gyr of
236 maturation and diagenesis. These sections have relatively low thermal overprints by Mesoproterozoic
237 standards, but they have experienced heating and pressurization, sufficient to reach the ‘dry gas’ window
238 ($\text{Ro}\%$ of 1.4) and expel most bitumens (Fustic et al., 2017). This process, referred to as ‘cracking,’ degrades

239 aliphatic monosulfide and disulfide bonds and, by $R_o\% \sim 1.5$, generates thiophenic sulfur in artificial
240 maturation and heating experiments (Sarret et al., 2002; Amrani et al., 2005; Kelemen et al., 2012).
241 Cracking and bitumen generation reduce the total amount of organic S remaining in kerogen by as much as
242 6–7-fold (Amrani et al., 2005) and can cause aromatization and other rearrangements within the remaining
243 sulfur-carbon backbone of the kerogen polymers (Rosenberg et al., 2017; Jin et al., 2021). Organic matter
244 in Arctic Bay shales thus records a likely restricted marine environment with nonetheless large reservoirs
245 of S, Mo, and trace metals, intermittently sulfidic and anoxic conditions (Hodgskiss et al., 2020), and
246 elevated primary productivity near coasts, the preservation of which was modified by heating and
247 maturation during diagenesis.

248

249 **2.2 Sample Collection and Storage**

250 Shale samples were collected from outcrops. To collect relatively ‘fresh’ samples, weathered surface
251 material was broken off using a geological hammer, and samples were then hammered off the outcrop.
252 Samples were stored in cloth sample bags so to allow moisture to escape and reduce weathering during
253 transportation and storage, while also minimizing contamination. Shale samples were trimmed with a
254 diamond saw to remove any remaining weathered portions. Samples were splits of the same powders
255 analyzed in Hodgskiss et al. (2020).

256

257 **2.3 Sequential Extractions and Kerogen Isolation**

258 Bitumen and elemental sulfur were microwave-extracted (MARS-6, CEM) from 2-gram powdered rock
259 samples twice in 20 mL of 9:1 dichloromethane:methanol (15 minutes at 70°C) at the University of
260 California, Santa Barbara (UCSB). Solvent extracts were evaporated under N_2 , visually inspected for S^0
261 crystals, and weighed. Remaining solids were then subjected to acid-volatile sulfide (AVS) and chromium-
262 reducible sulfide (CRS) extractions (Canfield et al., 1986) at Stanford University, after which solids,
263 extracts, and acid solutions were returned to UCSB. For both AVS and CRS extractions, sulfide gas was
264 trapped in 5% zinc acetate solution, washed, oxidized to sulfate in 30% hydrogen peroxide, and quantified
265 as dissolved sulfate by ion chromatography (Metrohm 930 IC / 889 with Metrosep A Supp 7 150 x 4.0 mm
266 anion column) at UCSB. AVS was not detectable above process blanks and is not discussed further. CRS-
267 derived sulfates were precipitated with excess $BaCl_2$, washed, dried, and weighed for S-isotope analysis as
268 $BaSO_4$. Organic matter in CRS-extracted solids is considered ‘kerogen’ and was subdivided for elemental
269 ratio, S-isotope, and X-ray absorption spectroscopy analyses. Carbon and sulfur contents of CRS-extracted
270 sediments were measured via combustion on an Eltra CS-500 analyzer at the University of California
271 Riverside (UCR). Both C wt% and S wt% were calibrated using Alpha Resources standard AR-4019 (C

272 wt% = 0.102, $1\sigma = 0.008$ and S wt % = 0.100, $1\sigma = 0.005$). During analysis, the measured precision (1σ)
273 of AR-4019 was 0.007 wt% for C and 0.004 wt% for S.

274

275 **2.4 Sulfate precipitation**

276 Inorganic sulfates were solubilized during the AVS extraction in anoxic, hot (60°C) 6N hydrochloric acid
277 and were separated from insoluble solids by centrifugation and decanting. Acid extracts were diluted
278 fivefold into ultrapure (milli-Q) water and combined with excess saturated BaCl₂ solution for ~12 hours to
279 precipitate sulfate as BaSO₄. Precipitates were centrifuged and washed 4x in ultra-pure water before
280 weighing and S-isotope analysis.

281

282 **2.5 Pyrite triple-isotope analyses**

283 Sulfur isotope analyses of pyrites were conducted in the McGill Stable Isotope Laboratory following
284 standard methods (Kunzmann et al., 2017). Samples were washed with ultra-pure water (milli-Q), dried
285 and crushed in a chrome-steel ringmill. Powdered samples (~0.2–15 g depending on S content) were placed
286 into a vessel, flushed with N₂(g), and subjected to CRS extraction as above (Canfield et al., 1986). The
287 H₂S(g) generated was carried in an N₂ stream and bubbled into a 4% zinc acetate solution to convert H₂S(g)
288 to ZnS(s). The ZnS(s) was converted to Ag₂S through the addition of 1 mL of 1 M AgNO₃. Samples were
289 filtered and then dried in an oven at ~80°C. For sulfur isotope analysis, 3 mg of Ag₂S were weighed into
290 aluminum foil packets which were then placed into nickel bombs. Samples were reacted under
291 a fluorine gas (F₂) atmosphere at 250 °C for 12 h to convert Ag₂S(s) to sulfur hexafluoride gas (SF₆[g]). The
292 resulting SF₆ gas was then purified progressively along a vacuum line through multiple cold-traps under
293 vacuum, followed by gas chromatography. Purified samples were analyzed in dual inlet mode on a Thermo
294 MAT-253. Results were measured against international standard reference material IAEA-S1 ($\delta^{34}\text{S} = -$
295 0.3‰ and $\Delta^{33}\text{S} = -0.061$). Estimated maximum errors (1σ) on measurements and the entire analytical
296 procedure are 0.1‰ for $\delta^{34}\text{S}$ and 0.01‰ for $\Delta^{33}\text{S}$.

297

298 **2.6 Multi-phase sulfur-isotope analyses**

299 Sulfur isotope analyses for CRS extracts (as BaSO₄), sulfates (as BaSO₄), and post-CRS residuals (kerogen)
300 were performed at UCR in the Lyons Biogeochemistry Laboratory with a Thermo Scientific Delta V Plus
301 continuous-flow stable isotope ratio mass spectrometer (IRMS). Sulfur from all sample types was converted
302 to SO₂ and separated via gas chromatography on a Costech ECS 4010, with gas flow to the IRMS being
303 controlled by a Thermo Scientific ConFlo III open split interface. Kerogens were bracketed by the
304 international measurement standards IAEA-S1 (-0.30‰), IAEA-S2 (22.67‰), and IAEA-S3 (-32.55‰);
305 BaSO₄ samples were bracketed by IAEA-SO5 (0.49‰), IAEA-SO6 (-34.05‰), and NBS-127 (21.1‰).

306 Precision of standards (1σ) was 0.9‰ or better for all kerogen analyses and 0.4‰ or better for all BaSO₄
307 analyses.

308

309 **2.7 X-ray absorption spectroscopy**

310 The redox speciation and bonding environment of sulfur in whole and CRS-extracted sediments were
311 analyzed at beam line 14-3 at the Stanford Synchrotron Radiation Lightsource (SSRL). Powdered samples
312 were mounted on St Gobain M60 S-free polyester tape and covered in 5- μ m-thick SPEX 3520
313 polypropylene XRF film. XAS spectra were collected from 2460 to 2540 eV (Fig. S1), as calibrated to the
314 thiol pre-edge peak of thiosulfate at 2472.02 eV. The X-ray beam was trimmed to a size of 500 x 500 μ m
315 at a flux of $\sim 8 \times 10^{10}$ photons per second. Beam line 14-3 is equipped with a Si(111) ($\Phi = 90$) double crystal
316 monochromator, and the S K α fluorescence line is measured with a Si Vortex Si drift detector (Hitachi)
317 using Xspress3 pulse processing electronics (Quantum Detectors). Sulfur XAS spectra were processed in
318 the SIXPACK (Webb, 2005) software package using a K-edge E^0 of 2473 and pre-edge and post-edge linear
319 normalization ranges of -20 to -7 and 35 to 70 eV, respectively. Spectra were fit to a set of eight organic
320 and six inorganic standard spectra (Fig. S2), which are presented grouped by major functional type:
321 aromatics (dibenzothiophene, thianthrene), alkyl sulfides (methionine), alkyl disulfides (phenylene
322 disulfide, glutathione disulfide), sulfoxides (methionine sulfoxide), sulfonates (cysteic acid), organic sulfate
323 esters, elemental S, pyrite, iron monosulfides (mackinawite, pyrrhotite), and sulfates (sodium sulfate,
324 gypsum).

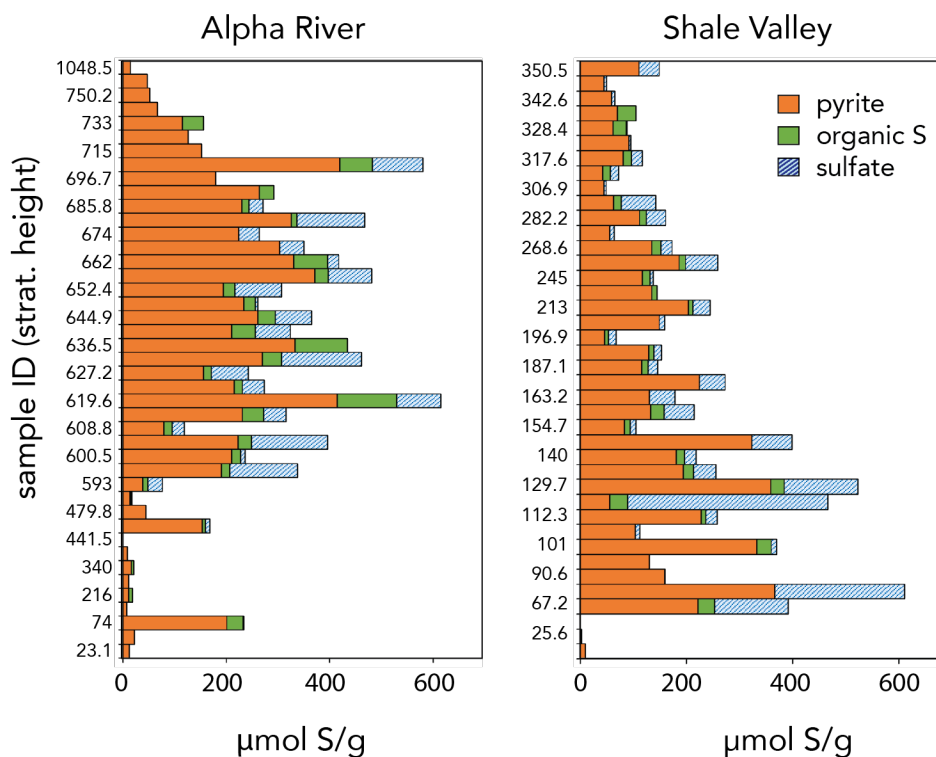
325

326

327 **3. RESULTS**

328

329 **3.1 Concentrations of sulfur phases**



330
 331 **Fig. 2 - Concentrations of pyrite, organic S, and inorganic sulfate in Arctic Bay Formation black**
 332 **shales.** Data are from sequential chemical extractions. Samples are arranged by stratigraphic height order;
 333 every-other sample ID is shown for legibility (Table S1). Total sulfur is primarily pyrite, although a few
 334 samples contain more acid-soluble sulfate than pyrite. Total sulfur in both sections includes an average of
 335 approximately 16% acid-soluble sulfate and 11% organic S.

336
 337 Alpha River samples contain between 7 and 420 $\mu\text{mol S}_{\text{py}}/\text{g}$ (0.04 to 2.5 wt% FeS_2), and Shale Valley
 338 samples contain between 2 and 366 $\mu\text{mol S}_{\text{py}}/\text{g}$ (0.01 to 2.2 wt% FeS_2). Pyrite concentrations (Figure 2 and
 339 Table S1) are relatively high in the TOC-rich black shales from Alpha River and in some black shales from
 340 the lower part of the Shale Valley section. Pyrite concentrations reported here represent corrected versions
 341 of the data reported in Hodgskiss et al. (2020), which contained a calculation error. After pyrite, the second
 342 most abundant sulfur phase is acid-soluble sulfate, defined as sulfur that was solubilized in strong acid (6N
 343 HCl, 60°C, 2 hrs) and trapped as sulfate (with Ba^{2+}). Inorganic sulfate, carbonate-associated sulfate (CAS),
 344 and sulfate-rich minerals like gypsum and phosphates are also trapped as part of this acid-soluble pool, as
 345 are some organic sulfate esters. Visible BaSO_4 precipitates formed in 58 of the 82 total sample extracts and
 346 represented concentrations of up to 155 $\mu\text{mol S}_{\text{so4}}/\text{g}$ in Alpha River and up to 377 $\mu\text{mol S}_{\text{so4}}/\text{g}$ in Shale
 347 Valley. Organic (kerogen) sulfur concentrations ranged from < 0.2 to 115 $\mu\text{mol S}_{\text{org}}/\text{g}$ in Alpha River and
 348 from 0.4 to 91.4 $\mu\text{mol S}_{\text{org}}/\text{g}$ at Shale Valley. Organic solvent extractions did not yield detectable bitumen

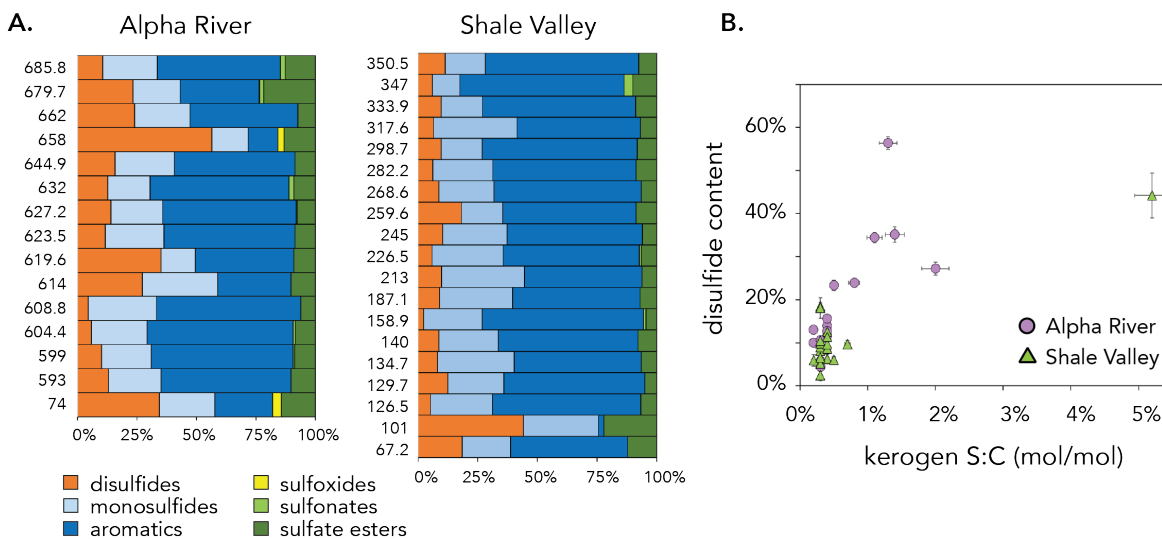
349 or elemental S. Published total S concentrations from splits of these same samples (Hodgskiss et al., 2020)
 350 are an average of 22% higher than the sum of phases recovered in the current study. Missing S in this mass
 351 balance could have been present as acid-soluble, non-Ba-reactive organic S or could have been lost during
 352 the manual transfer of BaSO₄ powders for weighing and/or during CRS recovery (typically ~93-99%
 353 efficient; Canfield et al., 1986). Sulfur was not detected in the acid-volatile (AVS) or organic solvent-
 354 extracted (lipid/S⁰) pools.

355
 356 Consistent with published datasets (Table S1), TOC concentrations in Alpha River averaged 4.1 mmol
 357 C_{org}/g (5.0 wt% TOC) and ranged from 0.5 to 11.3 mmol C_{org}/g (0.6 to 13.6 wt% TOC). In Shale Valley,
 358 TOC concentrations averaged 5.7 wt% and ranged from 0.7 to 12.3 wt%. The molar sulfur-to-carbon (S:C)
 359 ratios of this organic matter average 0.8 mol% (S:C = 0.8 : 100 mol/mol) in Alpha River and 0.6 mol% in
 360 Shale Valley. S:C ratios of ≥2.0 mol% were found in just four samples from Alpha River and two samples
 361 from Shale Valley; the absence of pyrite in these kerogens was confirmed by XAS.

362

363 3.2 X-ray absorption spectroscopy

364



365

366

367 **Fig. 3 – Speciation of organic S in Arctic Bay kerogens.** A: Organic sulfur species are ordered from most
 368 reduced (left) to most oxidized (right). Fitting errors on each component are typically 1-2% (Table S1). B:
 369 Relationships between kerogen S:C ratio and disulfide content for Alpha River (circles) and Shale Valley
 370 (triangles), showing elevated disulfide contents in S-rich samples. Only good-quality fits are shown (chi-
 371 squared values ≤ 30); see Table S1 for fit quality parameters and extended dataset.

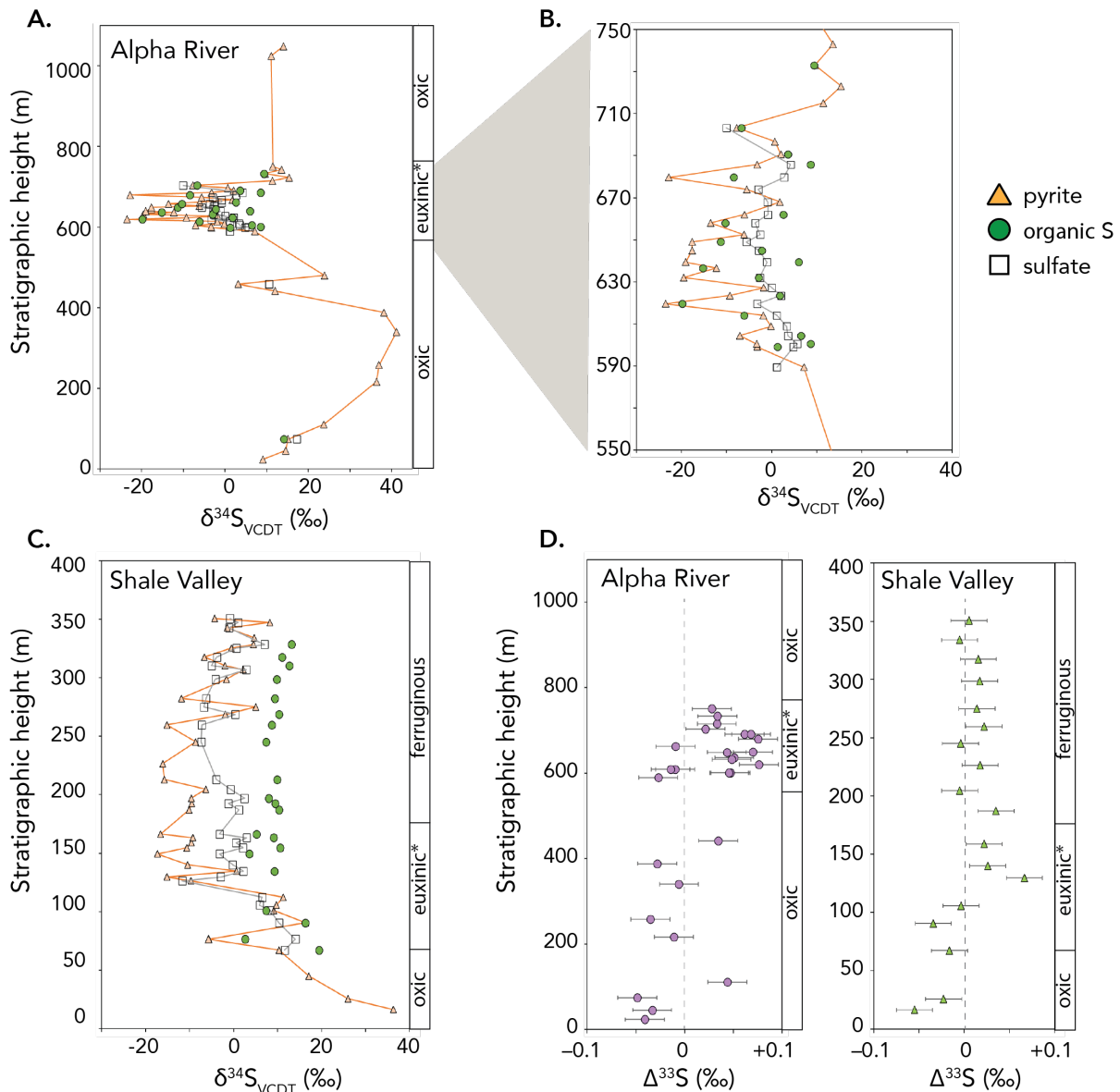
372

373 X-ray absorption spectroscopy (XAS) was conducted at SSRL to identify the speciation and redox state of
374 organic and total sulfur in shale samples (Figure 3 and Table S1). Kerogen sulfur (S_{org}) spectra were
375 collected for all rock powders containing measurable S. A subset of 16 samples was also measured by XAS
376 prior to sequential extractions to evaluate the distribution of sulfur phases before chemical treatments and
377 to assess the completeness of our mass balance. Consistent with Figure 2, whole rock sulfur spectra contain
378 variable proportions of pyrite, sulfate, and reduced organic sulfur as the major phases present (Table S1,
379 Fig. S1).

380
381 Organic sulfur in kerogen is on average 90.6% ‘reduced’; the remaining (oxidized) organic S best resembles
382 sulfate esters. A primary XAS feature at 2474.0 eV indicates aromatic organic sulfur moieties, similar to
383 dibenzothiophene but lacking its secondary structure at 2479 eV (Fig S1). Due to the energy overlap among
384 specific organic sulfur species in the 2473 – 2474 eV range and the signal-to-noise ratio of these spectra,
385 there is high uncertainty related to the relative abundances of aromatic versus monosulfide sulfur; in many
386 cases, fit quality parameters are only slightly less favorable when calculated with no organic monosulfide
387 component. In contrast, we can clearly distinguish between this primarily aromatic material and a feature
388 near 2472.4 eV that represents an organic S form with a lower effective ‘oxidation index,’ which is best fit
389 as disulfide (Vairavamurthy, 1998). Samples from Alpha River generally contain a larger proportion of
390 disulfide organic S (4 – 35%, averaging 16.5%) than those from Shale Valley (5 – 19%, averaging 10%).
391 The highest proportions of organic disulfides are present in samples with elevated S:C ratios (Fig. 3b), and
392 this trend continues with lower precision in lower-quality fits (Table S1).

393

394 **3.3 Sulfur-isotope compositions**



395
 396 **Fig. 4 - Stratigraphic profiles of sulfur-isotope compositions.** Panels A, B, and C show $\delta^{34}\text{S}$ values for
 397 pyrite (triangles), organic S (circles), and acid-soluble sulfate (open squares); panel B replicates data in (A)
 398 in higher resolution. Uncertainties are smaller than symbols ($\pm 0.4\text{‰}$ for pyrite and sulfate, $\pm 0.9\text{‰}$ for
 399 organics). Panel D shows the minor-isotope composition ($\Delta^{33}\text{S}$) of pyrite in both sections. Bars along the
 400 right-hand side of profiles show inferred local redox conditions, where ‘euxinic*’ indicates ambiguous
 401 and/or intermittent euxinic conditions (Hodgskiss et al., 2020).

402
 403

404 Sulfur-isotope compositions ($\delta^{34}\text{S}$ values) were measured for three coexisting sulfur phases in Arctic Bay
 405 shales: pyrite, kerogen, and acid-soluble sulfate. Pyrite $\delta^{34}\text{S}$ values range from -23.5‰ to $+41.2\text{‰}$ and

406 show coherent shifts across the sections. In Shale Valley, pyrite is strongly ^{34}S -enriched in the lowest part
407 of the section and becomes gradually more depleted ($-10\text{‰} \pm 10\text{‰}$) by 125 m stratigraphic height. Pyrite
408 $\delta^{34}\text{S}$ values return to slightly higher values in the upper part of the section (275–350 m) but never exceed
409 $+8.2\text{‰}$. In the Alpha River section, large, coherent $\delta^{34}\text{S}$ shifts and strongly ^{34}S -enriched values characterize
410 the lower, less-TOC-rich part of the section (≤ 550 m), with a maximum $\delta^{34}\text{S}$ value of $+41.2\text{‰}$ at 340 m. In
411 contrast, all pyrite $\delta^{34}\text{S}$ values between 593 and 686 m are moderately ^{34}S -depleted, with values between –
412 23.5 and $+1.8\text{‰}$ (Fig. 4). Pyrite in the upper Alpha River section (>710 m) has an intermediate S-isotope
413 composition ranging from $+9.6$ to $+15.4\text{‰}$.

414
415 The isotopic composition of organic sulfur ranges from -19.8 to $+14.1\text{‰}$ at Alpha River and from $+9.7$ to
416 $+19.4\text{‰}$ at Shale Valley (Fig. 4 and Table S1). Organic S at Alpha River is generally more ^{34}S -depleted
417 than at Shale Valley, and the average $\delta^{34}\text{S}$ difference between pyrite and organic S (ϵ_{PK}) is smaller at Alpha
418 River (6.3‰) than at Shale Valley (15.0‰). At the same time, maximum ϵ_{PK} values for individual samples
419 are similar at both sites (25.0‰ and 25.6‰ , respectively; Fig. 3, Table S1). Organic S is slightly more ^{34}S -
420 depleted than pyrite, by as much as 4.3‰ , in 5 of 24 samples at Alpha River and 2 of 21 samples at Shale
421 Valley. Samples with this relatively atypical, reversed S-isotope pattern (Vairavamurthy et al., 1995) are
422 scattered throughout both sections and associated with pyrites that are generally ^{34}S -enriched relative to
423 surrounding layers, consistent with the addition of ^{34}S -enriched, later-stage pyrite.

424
425 Sulfate $\delta^{34}\text{S}$ values fall within the same range as organic sulfur and pyrite throughout the sections, ranging
426 from -11.7 to $+17.2\text{‰}$ and averaging $+0.5\text{‰}$. Sulfate $\delta^{34}\text{S}$ values show a close relationship with pyrite $\delta^{34}\text{S}$
427 in some parts of the sections. In the upper part (>250 m) in the Shale Valley section, for example, both
428 parameters vary in concert and remain within 5‰ of each other. Such isotopic agreement often points to
429 pyrite oxidation as the source of (secondary) sulfate (see details in the Discussion below). Other parts of
430 the sections preserve larger offsets between the two pools – for example, at Shale Valley between 130 and
431 250 m – where sulfate $\delta^{34}\text{S}$ values are on average 10.4‰ (range 5.9 to 14.8‰) more ^{34}S -enriched than
432 coexisting pyrite. Sulfate $\delta^{34}\text{S}$ values show less variability than pyrite $\delta^{34}\text{S}$ values through the Alpha River
433 shales between 590 and 710 m.

434
435 The minor-isotope ($\Delta^{33}\text{S}$) composition of pyrite ranges from -0.05‰ to $+0.08\text{‰}$ (Fig. 3d). Many Shale
436 Valley values are near zero (average $+0.01\text{‰}$). Minimum $\Delta^{33}\text{S}$ values (-0.05‰) are found in the lower,
437 apparently oxic portions of both sections, alongside ^{34}S -enriched pyrites. Pyrite $\Delta^{33}\text{S}$ values are significantly
438 greater than zero (average $+0.04\text{‰}$) in many samples deposited under apparently intermittently sulfidic

439 conditions, including many samples from Alpha River between 590-690 m and one sample from Shale
440 Valley (129.7 m, +0.07‰).

441

442 4. DISCUSSION

443

444 4.1 Sulfate sources and implications for iron speciation

445 Sulfate in sedimentary rocks is often derived from seawater sulfate, whether it is present as an evaporative
446 salt mineral like gypsum (CaSO_4) or incorporated within the crystal lattice of a carbonate mineral (i.e.,
447 carbonate-associated sulfate, or CAS). Seawater-derived sulfates in both forms are well known from the
448 Iqqittuq and Angmaat formations, overlying the Arctic Bay Formation, where the $\delta^{34}\text{S}$ of evaporative
449 gypsum layers is $\sim +22\text{‰}$ (Kah et al., 2001, 2004; Johnston et al., 2005) (Fig. 1). These sulfate S-isotope
450 compositions serve as our best estimate for basin seawater sulfate $\delta^{34}\text{S}$ during Arctic Bay deposition. Unlike
451 CAS and gypsum minerals in overlying strata, acid-soluble sulfates from Arctic Bay Formation shales have
452 distinctively ^{34}S -depleted compositions that are similar to coexisting pyrite and organic S, which indicates
453 that the primary source of sulfate to Arctic Bay rocks is the oxidation of pyrite and/or organic sulfur.

454

455 Pyrite oxidation during the weathering of shales is well known and can extend tens of meters below the
456 outcrop surface (Gu et al., 2020). Pyrite oxidation can also occur during sample handling. During pyrite
457 oxidation by O_2 , sulfur is oxidized to sulfate while ferrous iron is oxidized to Fe^{3+} . In shales that contain
458 sufficient carbonates to buffer against acid accumulation and related Fe^{3+} solubility, the ferric iron (Fe^{3+})
459 produced by pyrite oxidation is generally retained as oxide mineral phases (Pye and Miller, 1990; Brantley
460 et al., 2013; Mahoney et al., 2019). Arctic Bay shales contain abundant carbonates (averaging 39 wt%), so
461 they were presumably pH-buffered during pyrite oxidation and are unlikely to have experienced substantial
462 iron loss. This assumption is important for our understanding of Fe_{HR} concentrations (see below).

463

464 Unlike iron, the sulfate produced during pyrite oxidation can either be mobile in oxidizing fluids or retained
465 as gypsum (CaSO_4), in phosphates, or as jarosite ($\text{KFe}_3(\text{SO}_4)_2(\text{OH})_6$) (Chandra and Gerson, 2010). Elevated
466 concentrations of acid-soluble sulfate were present in nearly all samples with moderate-to-high pyrite
467 concentrations (Fig. 2), yielding a rough positive association between pyrite and sulfate concentrations (Fig.
468 S3). The close correspondence between pyrite and sulfate $\delta^{34}\text{S}$ values in the upper part of the Shale Valley
469 section indicates that acid-soluble sulfates derived primarily from local S_{py} oxidation (Fig. 4). In the
470 densely-sampled, TOC-rich Alpha River shales between 600-700 m, however, sulfate $\delta^{34}\text{S}$ values are less
471 variable and an average of 9.7‰ higher than pyrite $\delta^{34}\text{S}$ values. Mixing with ^{34}S -enriched sulfate from
472 evaporites is unlikely to explain this S-isotope difference because we lack lithological evidence for

473 subaerial exposure or related evaporite deposition in these sections (see Fig. 1 for regional evaporite
474 locations). Potential contributions from CAS are also small: if CAS were present at a concentration of 100
475 ppm in carbonate in these shales (Kah et al., 2004), it would account for an average of 0.7% of observed
476 acid-soluble sulfate concentrations (see Table S1). Instead, the differences between pyrite and sulfate $\delta^{34}\text{S}$
477 values in TOC-rich Alpha River shales (600-700 m) could reflect contributions to the acid-soluble sulfate
478 pool from the local oxidation of abiogenic organic sulfur (Petsch et al., 2000) and/or sulfate mobilized from
479 pyrite oxidation in under- and overlying layers (Fig. 4).

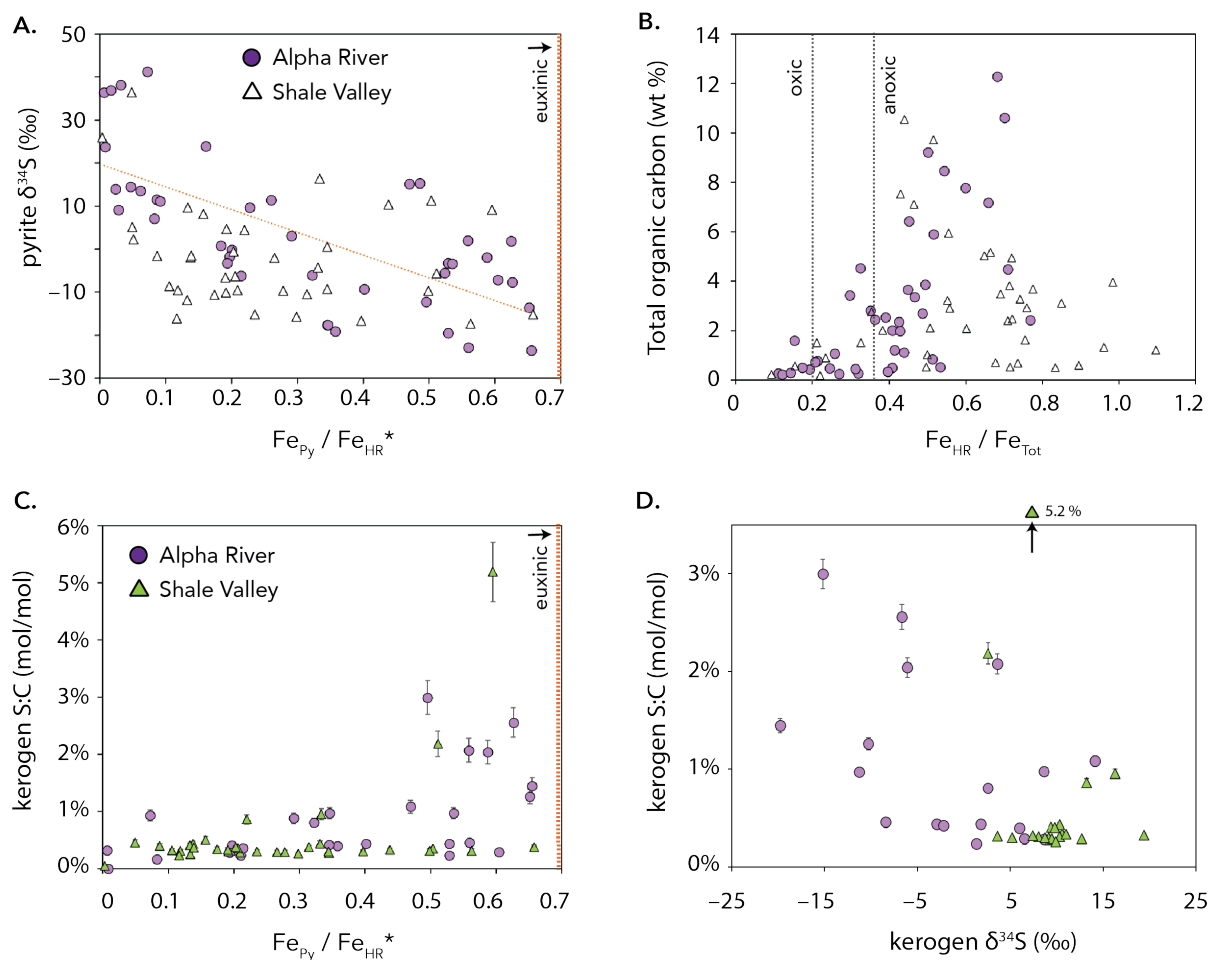
480
481 Both pyrite (FeS_2) and its oxidation products like $\text{Fe}(\text{OH})_3$ are considered ‘highly reactive iron’ or Fe_{HR}
482 (Canfield, 1989). If the iron oxidized during pyrite oxidation is retained locally (<mm-scale), this
483 transformation has no effect on the $\text{Fe}_{\text{HR}}/\text{Fe}_{\text{T}}$ ratio used to classify environments as oxic or anoxic (Mahoney
484 et al., 2019). However, pyrite oxidation can decrease the ratio $\text{Fe}_{\text{Py}}/\text{Fe}_{\text{HR}}$, which is used to determine whether
485 environments were sulfidic (Poulton and Canfield, 2005; Raiswell et al., 2018). If we assume that total acid-
486 soluble sulfates represent solely the products of local pyrite oxidation and that no Fe_{HR} was diagenetically
487 transferred to the unreactive pool, we can estimate original $\text{Fe}_{\text{Py}}/\text{Fe}_{\text{HR}}$ ratios prior to pyrite oxidation (Fig.
488 S4). These values are minima if sulfate loss exceeded sulfate gain, although the scale of sulfate mobilization
489 is poorly constrained. Still, corrected values should more closely resemble initial ratios for $\text{Fe}_{\text{Py}}/\text{Fe}_{\text{HR}}$ than
490 uncorrected values. Reconstructed $\text{Fe}_{\text{Py}}/\text{Fe}_{\text{HR}}$ ratios (Fig. S4) are slightly higher than those originally
491 reported in Hodgskiss et al. (2020), but maximum $\text{Fe}_{\text{Py}}/\text{Fe}_{\text{HR}}$ ratios of 0.66 in both sections still fall below
492 the canonical euxinic threshold (Poulton and Canfield, 2005).

493

494 **4.2 Pyrite isotope patterns and local redox conditions**

495 The S-isotope composition of pyrite is a complex function of overlapping biogeochemical and
496 sedimentological processes within and overlying the sediment column. A principal driver of S-isotope
497 patterns in the environment is the strong fractionation imparted by sulfate reducing microorganisms, which
498 preferentially use lighter S-isotopes, producing ^{34}S -depleted sulfide and driving residual sulfate toward
499 higher $\delta^{34}\text{S}$ values. Variations in the fractionation factor associated with microbial sulfate reduction (MSR)
500 can thus impact the $\delta^{34}\text{S}$ values of sulfide and its products. For example, apparent fractionation factors
501 during MSR can decrease in response to higher-quality OM sources and correspondingly elevated cell-
502 specific metabolic rates (Chambers et al., 1975; Leavitt et al., 2013). Strongly ^{34}S -depleted pyrite (<-20‰)
503 is typically formed in environments that host microbial sulfate reduction in the water column or very
504 shallow sediments, where sulfate is replete due to the large seawater reservoir or efficient diffusive
505 exchange with the immediately overlying water column, respectively (Lyons, 1997; C. Li et al., 2010;
506 Pasquier et al., 2017; Raven et al., 2018; Houghton et al., 2022). As the rate of sulfate supply decreases

507 relative to the rates of sulfate reduction and pyrite formation, for example in more deeply buried sediments,
508 environments tend to record smaller differences between the $\delta^{34}\text{S}$ values of seawater sulfate and
509 sedimentary pyrite (Zaback et al., 1993; Fike et al., 2015; Liu et al., 2021). Microbial sulfate reduction in
510 OM-rich sediments thus generates profiles approximating Rayleigh distillation, with declining pore water
511 sulfate concentrations and increasing sulfate $\delta^{34}\text{S}$ values with depth (Jorgensen, 1979). Not all ^{34}S -enriched
512 pyrites form in deep sediments, however. Strongly ^{34}S -enriched sedimentary pyrites, including some with
513 $\delta^{34}\text{S}$ values exceeding seawater sulfate, are found in modern, shallow-water sediments that experience
514 episodic deposition, oxidative reworking, and other non-steady-state processes, especially in the presence
515 of reactive iron minerals (Aller et al., 2010). Freshwater lakes or restricted marine basins with low sulfate
516 concentrations can also develop isotopically distinctive sulfate reservoirs, depending on the relative rates
517 of microbial sulfate reduction versus sulfate replenishment (Lyons et al., 2000). During heating and
518 catagenesis, organic S breakdown in the presence of iron (Amrani et al., 2005; Siedenberg et al., 2018; see
519 below) can also contribute to pyrite $\delta^{34}\text{S}$ values. Pyrite has been shown to reductively degrade in higher
520 stages of thermal maturation in experimental settings, especially in the presence of H_2 and water, but natural
521 systems like the Arctic Bay shales are unlikely to result in a pyrite decomposition regime (Rosenberg et al.,
522 2017).
523



524
 525 **Fig. 5 – Redox state / organic matter relationships.** (a) Relationship between the redox indicator for
 526 ferruginous-to-sulfidic conditions, $\text{Fe}_{\text{Py}}/\text{Fe}_{\text{HR}}$, and the S-isotope composition of pyrite. Iron ratios are
 527 reconstructed (*) to account for pyrite oxidation based on Hodgskiss et al. (2020), as shown in Figure S4.
 528 The regression line ($R^2 = 0.38$) applies only to data from Alpha River (purple circles). (b) Relationship
 529 between the redox indicator for oxic-to-anoxic conditions, $\text{Fe}_{\text{HR}}/\text{Fe}_{\text{T}}$ (Hodgskiss et al., 2020), and total
 530 organic carbon (TOC) concentrations, showing canonical thresholds for oxic, anoxic, and ambiguous redox
 531 conditions (Poulton and Canfield, 2005). (c) Relationship between $\text{Fe}_{\text{Py}}/\text{Fe}_{\text{HR}}$ and the S:C ratio of kerogen.
 532 (d) Relationship between the S-isotope composition and S:C ratio of kerogen; note the adjusted y-axis
 533 relative to (c).

534
 535 Pyrite is relatively ^{34}S -enriched at the bottom of both Arctic Bay sections (Fig. 3), with some pyrite $\delta^{34}\text{S}$
 536 values exceeding estimates for basin seawater sulfate (Kah et al., 2001; Crockford et al., 2019). Throughout
 537 this lower interval, trace metals, iron speciation, and lithologies are consistent with deposition under oxic
 538 water column conditions (Hodgskiss et al., 2020). Therefore, relatively ^{34}S -enriched pyrite could indicate

539 that the sulfidic front and thus the location of pyrite formation were relatively deep in the sediments.
540 Alternatively, and especially at the shallower-water Alpha River site, ³⁴S-enriched pyrite could also stem
541 from episodic, oxidative reworking and rapid pyritization in near-surface sediments. In either case, ³⁴S-
542 enriched pyrite compositions support the interpretation that the overlying water column was not sulfidic
543 during the deposition of stratigraphically lower, relatively TOC-lean Arctic Bay Formation shales.

544
545 Pyrite is relatively ³⁴S-depleted in both sections during intervals characterized by more TOC-rich black
546 shales (600-700 m at Alpha River and above 125 m at Shale Valley). More ³⁴S-depleted pyrite likely reflects
547 a shallowing of the redox interface into very shallow sediments or the water column associated with more
548 reducing local environmental conditions. This interpretation is consistent with reported depletions in barium
549 concentrations across these intervals compared with surrounding strata (Hodgskiss et al., 2020). At Alpha
550 River, ³⁴S-depleted pyrites are weakly correlated with reconstructed iron speciation indicators for more
551 reducing (possibly sulfidic) conditions (Figure 5a). Trace metals and iron speciation at Shale Valley
552 (Hodgskiss et al., 2020) also broadly suggest an association between more ferruginous to possibly sulfidic
553 conditions and ³⁴S-depleted pyrite. Overall, pyrite S isotopes appear to record a shift in the location of sulfur
554 cycling and pyrite formation between deeper (and/or reworked) sediments during oxygenated periods and
555 shallower sediments (and/or the water column) during more reducing periods.

556
557 Minor sulfur isotope ratios ($\Delta^{33}\text{S}$) can help distinguish among processes with slightly different mass
558 fractionation relationships, for example microbial sulfate reduction ($\lambda \sim 0.515$) and sulfur
559 disproportionation (Johnston et al., 2005; Kunzmann et al., 2017). The latter has a stronger relative
560 preference for ³³S and generates sulfate with $\delta^{33}\text{S}$ values that are higher than those expected in an
561 environment hosting only microbial sulfate reduction (Bradley et al., 2016). Rocks overlying the Arctic
562 Bay Formation shales (Angmaat Formation) contain carbonate-associated sulfate that is slightly ³⁴S-
563 enriched relative to near-coeval gypsum layers and has a resolvable $\Delta^{33}\text{S}$ enrichment (up to $0.07 \pm 0.02\%$)
564 that Johnston et al. (2005) interpreted as requiring sulfur disproportionation. However, the subsequent
565 recognition of the expanded range of possible sulfur isotope fractionations ($^{34}\epsilon_{\text{MSR}}$) at low cell-specific
566 sulfate reduction rates (Sim et al., 2011) leaves the role of disproportionators ambiguous. In the Arctic Bay
567 Formation, pyrite $\Delta^{33}\text{S}$ compositions are systematically positive in intervals interpreted as intermittently
568 sulfidic, where pyrite is generally abundant and ³⁴S-depleted (Fig. 4). This pattern is widely observed as a
569 result of microbial sulfate reduction in modern sulfate-replete environments (Canfield et al., 2010; Zerkle
570 et al., 2010; X. Li et al., 2010) and is consistent with previous findings exploring Proterozoic sulfur cycling
571 (Kunzmann et al., 2017). The appearance of relatively ³³S-enriched, ³⁴S-depleted pyrite in the Arctic Bay
572 Formation supports the presence of sulfate concentrations >1 mM (Harrison and Thode, 1958; Johnston,

573 2005), in agreement with estimates based on rates of sulfate isotope variation in overlying strata (up to 4.5
574 mM; Kah et al., 2004). In contrast, small and consistent fractionations between carbonate-associated sulfate
575 and pyrite in earlier Mesoproterozoic sections have been interpreted to reflect sulfate concentrations \ll 1
576 mM (~1.7 – 1.4 Ga; Luo et al., 2015). To the extent that the Borden Basin records global marine chemistry,
577 it suggests that marine sulfate concentrations may have significantly increased during the Mesoproterozoic,
578 between ~1.4 and ~1.05 Ga, or that factors other than low sulfate concentrations led to the small apparent
579 fractionations in the early Mesoproterozoic.

580

581 **4.3 Organic sulfur formation and local redox conditions**

582 Organic sulfur in Alpha River shales is isotopically similar to coexisting pyrite and is strongly ^{34}S -depleted
583 relative to estimates for late Mesoproterozoic seawater, so it primarily represents the products of abiotic
584 sulfurization in the water column or shallow sediments. OM sulfurization therefore occurred at
585 approximately the same time as pyritization at the shallower-water, more shelf-like site. In contrast, organic
586 S is consistently more ^{34}S -enriched at Shale Valley, suggesting later diagenetic sulfurization in the deeper
587 basin.

588

589 Overall, these paired $\delta^{34}\text{S}_{\text{py}}$ and $\delta^{34}\text{S}_{\text{ker}}$ values for Arctic Bay shales overlap with the broad-scale patterns
590 observed in Phanerozoic O_2 -limited environments (Vairavamurthy et al., 1995; Raven et al., 2019) and
591 provide the first isotopic records of syngenetic-to-early-diagenetic OM sulfurization (sulfurization in the
592 water column or shallow sediments) in the Proterozoic. A handful of paired pyrite and organic S data have
593 been published for shales and dolostones from significantly younger (Neoproterozoic; 850-500 Ma)
594 sections, but these samples are strongly ^{34}S -enriched, with S_{org} values between 8.5 and 50.6‰, and likely
595 reflect relatively later diagenetic formation in diffusively restricted sediments during atypical conditions
596 linked to the global recovery from a Snowball Earth (Gorjan et al., 2000; Cai et al., 2022). Going further
597 back in Earth history, OM sulfurization was also identified in one study of an Archaean microbial mat.
598 There, organic S was isotopically similar to pyrite, with $\delta^{34}\text{S}$ values sometimes less than -15% , suggesting
599 early diagenetic sulfurization (Bontognali et al., 2012). Arctic Bay Formation kerogens thus help fill a more
600 than two-billion-year gap in our record of organic S across Earth history. As the first example of syngenetic-
601 to-early-diagenetic sulfurization of kerogens in an anoxic Proterozoic basin, they confirm that sulfur in
602 Proterozoic TOC-rich shales may represent the products of OM sulfurization reactions in the water column
603 or shallow sediments.

604

605 Elemental ratios of sulfur and carbon can complement isotopic evidence for OM sulfurization. Sulfurization
606 of highly functionalized organic matter can increase the sulfur content of kerogen relative to primary algal

607 and/or bacterial biomass, which has an initial S:C ratio near ~1 mol% (S:C = 1:100 mol/mol; Matrai and
608 Eppley, 1989; Chen et al., 1996). Kerogen S:C ratios therefore represent a rough indicator of sulfurization
609 intensity, at least for immature samples. Maturation and catagenesis cause the preferential loss of organic
610 S relative to C and will lower kerogen S:C ratios. Catagenesis of the Arctic Bay Formation shales exceeded
611 the oil and dry gas windows ($R_o\% = 1.4$, see Site Description), so we expect that significant amounts of
612 organic sulfur, especially aliphatic sulfides and disulfides, have been preferentially lost and that measured
613 S:C ratios are lower than original S:C ratios by a factor of as much as 6–7 (Amrani et al., 2005; Kelemen
614 et al., 2012). However, sulfide loss from kerogen during heating appears to be unidirectional, and
615 catagenesis does not cause the incorporation of pyrite sulfur into kerogens (Kelemen et al., 2012). In this
616 context, most Arctic Bay Formation kerogen S:C ratios are low (generally less than 1 mol%), in contrast to
617 prior suggestions that these ratios might exceed several tens of percent (Hodgskiss et al., 2020). However,
618 one sample from Shale Valley has an S:C ratio of 5.2 mol%, and five others have S:C ratios between 2 and
619 3 mol%. These S:C ratios resemble kerogen S:C ratios from modern and Phanerozoic anoxic and sulfidic
620 basins (Raven et al., 2019) and indicate that the OM available for sulfurization contained a substantial
621 concentration of sulfurizable functional groups. Therefore, it appears that predominantly microbial
622 Mesoproterozoic biomass has the potential to sulfurize to a roughly comparable extent as its Phanerozoic
623 equivalent.

624
625 Despite organic S loss during catagenesis, Arctic Bay Formation shales also appear to preserve some
626 relationships between S:C ratios, S-isotope compositions, and organic S speciation (by XAS). Unlike S:C
627 ratios, the bulk S-isotope composition of kerogen is unlikely to change substantially during breakdown and
628 S-loss, as substantial isotopic changes were not observed in oils or kerogens during heating in semi-open-
629 system kerogen maturation experiments (Amrani et al., 2005; Rosenberg et al., 2017). Kerogen S:C ratios
630 only exceed 2 mol% in samples with reconstructed Fe_{Py}/Fe_{HR} ratios above 0.5 (Fig. 5c), approaching but
631 not exceeding the canonical threshold used to infer sulfidic conditions in the water column. Higher S:C
632 ratios are also associated with more ^{34}S -depleted kerogens (Fig. 5d), a pattern that may reflect early
633 sulfurization of relatively fresh, functionalized OM (Raven et al., 2018). Alpha River kerogens with high
634 S:C ratios also contain relatively large proportions of apparent organic disulfides (Fig. 3), which are
635 common OM sulfurization products (Kohnen et al., 1991; Amrani and Aizenshtat, 2004; Raven et al.,
636 2021b). Although these trends lack the clarity sometimes preserved in Phanerozoic sections, they
637 consistently point toward relatively extensive OM sulfurization in environments with generally ferruginous
638 to sulfidic (as opposed to oxic) water column conditions, most notably at the shallower Alpha River site.
639

640 In a marine system with a water column characterized as ferruginous based on trace metals or other proxies,
641 OM sulfurization in the water column will be limited by low sulfide availability. Sulfurization in these
642 systems therefore most likely occurred within restricted zones that facilitate the drawdown of reactive iron,
643 including shallow sediments, sulfidic wedges, or sinking marine particles, in analogy to anoxic sub-
644 environments in the modern predominantly oxygenated ocean. Although ferruginous conditions are not
645 intrinsically associated with a specific iron concentration, dissolved Fe^{2+} concentrations in the water column
646 must be sufficient to quantitatively titrate out sulfide as iron sulfide solids at interfaces with sulfidic
647 conditions and therefore may have been at micromolar levels (Scholz, 2018; van de Velde et al., 2020). If
648 anoxic, Fe^{2+} -rich water upwells into a shallower, sulfidic water mass, it is likely to cause extensive iron
649 sulfide formation at the iron-sulfide redox interface. In this scenario, extensive iron sulfide formation in the
650 water column might therefore have pushed pyrite formation to outcompete OM for sulfide, functionally
651 disfavoring early OM sulfurization (Shawar et al., 2018; Hartgers et al., 1997). This effect may contribute
652 to the relatively large $\delta^{34}\text{S}$ difference between pyrite and organic S throughout the ferruginous interval in
653 Shale Valley, where more ^{34}S -depleted pyrite suggests a syngenetic source, while relatively ^{34}S -enriched
654 organic S is consistent with later organic S formation in more diffusively-limited, sulfidic sediments.

655
656 Alternatively, relatively ^{34}S -enriched organic S in Shale Valley kerogen could reflect mixing with a
657 substantial amount of primary biogenic material derived from either exported phytoplankton or benthic
658 mats (Vairavamurthy et al., 1995). Unfortunately, in these dry-gas-window shales, we do not observe any
659 systematic distinction in kerogen S speciation (by XAS) between ^{34}S -depleted and ^{34}S -enriched kerogens,
660 because any speciation-based evidence for different source materials has been lost to diagenesis. However,
661 biogenic organic S was likely a smaller component of Mesoproterozoic kerogens than modern kerogens for
662 two reasons. First, amino acids, some of which are S-bearing, were likely to have been in especially high
663 demand as a fixed nitrogen source in a largely anoxic, denitrifying ocean (Michiels et al., 2017). And
664 second, relatively recalcitrant organic sulfate esters, such as the algal exudate fucoidan, were presumably
665 less abundant because they are primarily produced by eukaryotes, which were present in relatively low
666 abundances in the Mesoproterozoic (reviewed in Lyons et al., 2021). Therefore, although the potential for
667 biomass contributions cannot be excluded, we interpret Shale Valley kerogens primarily as records of the
668 $\delta^{34}\text{S}$ value of deeper sedimentary sulfides.

669

670 **4.4 Impacts of sulfurization on Proterozoic OM burial**

671 In many Mesozoic and more recent O_2 -limited environments, there is a positive relationship between
672 sulfurization intensity (S:C ratio) and sedimentary OM concentrations (Boussafir et al., 1995; Van Kaam-
673 Peters et al., 1998; Raven et al., 2018, 2019). Despite the apparent relationship between environmental

674 redox conditions and OM sulfurization intensity, samples from the Arctic Bay Formation do not exhibit
675 clear relationships between indicators of sulfurization intensity (S:C ratios, kerogen S-isotopes, or Fe_{Py}/Fe_{HR}
676 ratios) and total organic carbon concentrations (Fig. S5 and S6). Instead, TOC has a broadly positive but
677 scattered relationship with Fe_{HR}/Fe_T (Figure 5b), indicating that anoxic conditions facilitate enhanced TOC
678 preservation via mechanisms other than sulfurization, such as oxygen scarcity. Although sulfurization was
679 not the primary driver of elevated OM concentrations in Arctic Bay Formation black shales, it did occur,
680 and it may have contributed to the preservation of sedimentary TOC. Additional paired organic S and pyrite
681 records from less mature black shales are needed to evaluate the significance of sulfurization for Proterozoic
682 OM burial more broadly.

683
684 Sulfurization may have a different relationship with quantitative OM burial in Proterozoic environments
685 than in well-studied Mesozoic environments for multiple reasons. Differences in sedimentary TOC content
686 may be especially sensitive to local primary productivity due to differences between Proterozoic and
687 Phanerozoic macronutrient cycles. Modern anoxic water columns have lower rates of OM remineralization
688 and phosphate regeneration than oxic locations (Van Mooy et al., 2002; Keil et al., 2016), which in turn
689 reduces the availability of phosphate to fuel primary productivity in upwelling zones. If the efficiency of
690 nutrient recycling in deep water were substantially reduced, Proterozoic primary producers could have been
691 much more dependent on local inputs of river-sourced phosphate than modern environments, where, in
692 contrast, 99% of phosphate supplied to primary producers is regenerated (Kipp and Stüeken, 2017; Laakso
693 and Schrag, 2019). By this logic, the elevated OM burial in Arctic Bay shales could primarily reflect
694 elevated local sources of phosphate to this semi-restricted basin.

695
696 The effects of anoxic deep water on OM preservation may have been at least partly offset by differences in
697 particle dynamics in Proterozoic versus Phanerozoic ecosystems. In modern marine systems, rapidly
698 sinking particles are a key link connecting rapid OM sulfurization and sediment OM burial. Eukaryotic
699 primary producers can generate large, ballasted, often polysaccharide-rich particles that transfer OM rapidly
700 to the seafloor (Alldredge and Silver, 1988; Engel et al., 2004) or even host internally reducing
701 microenvironments (Canfield et al., 2010; Raven et al., 2021a), and eukaryotic zooplankton contribute to
702 the rapidly sinking particle flux through vertical migration and fecal pellet production (Turner, 2015). The
703 microbial ecosystems of the Mesoproterozoic would have lacked these mechanisms for efficient transport
704 of OM to the seafloor (Logan et al., 1995). This difference would have increased particulate OM ‘exposure
705 time’ to water column conditions (Hartnett et al., 1998), which are typically less reducing and therefore
706 more energetically efficient for respiring OM than the sediments. Slower particle sinking thus increases the
707 likelihood of microbial degradation and defunctionalization of sinking particulate OM during transit and

708 decreases the odds of exposure of reactive OM to sulfidic conditions in surface sediments. OM preservation
709 may thus have been relatively sensitive to changes in particle formation and sinking rates in the water
710 column and less sensitive to chemical transformations like sulfurization in shallow sediments. In this
711 framework, OM burial in Arctic Bay shales could be enhanced by local inputs of terrigenous ballast
712 materials that facilitate rapid particle delivery to the sediments.

713
714 Additionally, bacterial and archaeal biomass may be less intrinsically susceptible to sulfurization than algal
715 biomass due to chemical differences in the compositions of their biomass and exudates. To date,
716 sulfurization experiments and environmental studies have focused primarily on algal biomass and
717 biomarkers like steroids (Gelin et al., 1998; Kok et al., 2000a, b; Raven et al., 2021b). Similar reactions are
718 likely to impact major components of bacterial and archaeal biomass but are less well understood.
719 Moreover, given the high OM S:C ratios observed in some Arctic Bay shales (up to ~5.2 mol%, with the
720 absence of pyrite confirmed by XAS), OM in this environment is clearly sulfurizable under the right
721 conditions. Therefore, although we do not observe a correlation between apparent sulfurization intensity
722 and TOC concentrations, sulfurization could have played a role in bulk OM preservation in locally sulfidic
723 Proterozoic environments, as it does in younger systems. Similarly, sulfurization could have contributed to
724 the enhanced preservation of specific components of sedimentary OM, including organic fossils or
725 biomarkers, especially in other, less mature Proterozoic rocks (Kohnen et al., 1991; Rosenberg et al., 2018;
726 Olcott et al., 2022; Tingle et al., 2023).

727

728

729 5. CONCLUSIONS

730

731 A global change in organic matter (OM) burial efficiency remains a leading hypothesis to reconcile carbon
732 mass balance throughout Earth history (Kipp et al., 2021), and enhanced OM sulfurization could be a
733 contributing mechanism to explain TOC-rich rocks of the mid-Proterozoic. We find clear evidence that
734 sulfurization occurred during early sedimentation and diagenesis of black shales under ferruginous-to-
735 sulfidic conditions in the late Mesoproterozoic Arctic Bay Formation, Borden Basin (~1.05 Ga).
736 Sulfurization at a relatively shallow site (Alpha River) was broadly concurrent with pyrite formation and
737 generated strongly ³⁴S-depleted OM. Although the organic sulfur content of these shales has been reduced
738 by thermal cracking during later diagenesis, kerogens that retained elevated S:C ratios are relatively rich in
739 disulfides, both indicating more intense sulfurization. Kerogen S:C ratios as high as 5.2 mol% suggest that
740 Mesoproterozoic biomass was similar to modern algal biomass in terms of its density of potentially

741 sulfurizable functional groups, and that it could have been strongly sulfurized under the right conditions,
742 despite likely differences in major OM sources.

743

744 Although the shallow and deep sections of the Arctic Bay Formation have similar TOC and pyrite
745 concentrations, conditions in the deeper basin site (Shale Valley) appear to have suppressed early diagenetic
746 OM sulfurization. At that site, OM S-isotope compositions are relatively invariant and ^{34}S -enriched relative
747 to coexisting pyrite, suggesting that ferruginous conditions in the water column drove sulfurization
748 reactions deeper into the sediments.

749

750 Despite these observations, sulfurization intensity does not appear to be a primary driver of enhanced TOC
751 concentrations in the Borden Basin, contrasting with observations from well-studied Mesozoic and more
752 recent black shales. Instead, highly localized inputs of macronutrients and a phosphate-limited biosphere
753 may have tightly coupled sedimentary TOC concentrations to local productivity levels. Alternatively, OM
754 preservation efficiency may have been especially sensitive to processes impacting local particle fluxes and
755 electron acceptor exposure times. Nevertheless, OM sulfurization did occur during sedimentation or early
756 diagenesis, most notably during the deposition of TOC-rich shales at the shallower-water site, which means
757 that sulfurization in this Mesoproterozoic environment retains the potential to enhance the preservation of
758 specific components of OM (i.e., biomarkers, organic fossils) and to record valuable isotopic information
759 about ancient biogeochemical cycles. Organic sulfur is an important but still poorly understood component
760 of Earth's early sulfur cycle.

761

762

763

764 **Acknowledgements**

765 We thank A. Schartmann (University of California Santa Cruz) and K. O'Malley (University of California
766 Santa Barbara) for assistance with sample preparation, E.A. Sperling for assistance with Fe speciation
767 analyses, and G.P. Halverson, D. Cole, S. Wörndle, T.M. Gibson, and V. Cumming for assistance with
768 sample collection and field logistics. The hamlets of Pond Inlet and Arctic Bay, and the respective Hunters
769 and Trappers Associations, are thanked for their support to conduct this research.

770

771 Funding was provided through the UCSB Hellman Family Faculty Fellows Program (MRR) and the NASA
772 Interdisciplinary Consortia for Astrobiology Research (ICAR) Program (TWL). PWC and MSWH
773 acknowledge funding through an NSERC PGS-D, NSTP and NSERC CREATE CATP.

774

775 Use of the Stanford Synchrotron Radiation Lightsource, SLAC National Accelerator Laboratory (proposal
776 5359) is supported by the U.S. Department of Energy, Office of Science, Office of Basic Energy Sciences
777 under contract no. DE-AC02-76SF00515. The SSRL Structural Molecular Biology Program is supported
778 by the DOE Office of Biological and Environmental Research and by the National Institutes of Health,
779 National Institute of General Medical Sciences (P30GM133894).

780

781 **Research Data**

782 All of the processed data discussed in this manuscript are available as part of the Supplemental Tables
783 associated with this article. Data are also available online at FigShare (link populated on manuscript
784 acceptance).

785

786 **Appendix A. Supplementary Material**

787 Supplementary Material for this manuscript includes six figures, details about the calculation of corrected
788 Fe_{Py}/Fe_{HR} ratios, and complete data tables. Figures show (1) XAS spectra for kerogens and whole rock
789 samples; (2) XAS standard spectra used in fits; (3) reconstructed iron speciation profiles; (4) relationships
790 between pyrite and sulfate; (5) the relationship between TOC concentrations and the ratio of highly reactive
791 iron to total iron; and (6) relationships between total organic carbon TOC concentrations and indicators of
792 organic matter sulfurization intensity.

793

794

795 **References**

796 Alldredge A. L. and Silver M. W. (1988) Characteristics, dynamics and significance of marine snow.
797 *Prog. Oceanogr.* **20**, 41–82.

798 Aller R. C., Madrid V., Chistoserdov A., Aller J. Y. and Heilbrun C. (2010) Unsteady diagenetic
799 processes and sulfur biogeochemistry in tropical deltaic muds: Implications for oceanic isotope
800 cycles and the sedimentary record. *Geochim. Cosmochim. Acta* **74**, 4671–4692.

801 Amrani A. and Aizenshtat Z. (2004a) Mechanisms of sulfur introduction chemically controlled: $\delta^{34}S$
802 imprint. *Org. Geochem.* **35**, 1319–1336.

803 Amrani A. and Aizenshtat Z. (2004b) Reaction of polysulfide anions with α,β unsaturated isoprenoid
804 aldehydes in aquatic media: simulation of oceanic conditions. *Org. Geochem.* **35**, 909–921.

805 Amrani A., Ma Q., Ahmad W. S., Aizenshtat Z. and Tang Y. (2008) Sulfur isotope fractionation during
806 incorporation of sulfur nucleophiles into organic compounds. *Chem. Commun.*, 1356.

807 Amrani A., Lewan M.D., Aizenshtat Z. (2005) Stable sulfur isotope partitioning during simulated
808 petroleum formation as determined by hydrous pyrolysis of Ghareb Limestone, Israel.
809 *Geochimica et Cosmochimica Acta* **69**, 5317–5331.

- 810 Blackadar R. and Lemon R. (1963) Admiralty Inlet area. *Baffin Isl. Dist. Frankl. Geol. Surv. Can. Mem.*
811 **328**, 84.
- 812 Blättler C. L., Bergmann K. D., Kah L. C., Gómez-Pérez I. and Higgins J. A. (2020) Constraints on
813 Meso- to Neoproterozoic seawater from ancient evaporite deposits. *Earth Planet. Sci. Lett.* **532**,
814 115951.
- 815 Bontognali T. R. R., Sessions A. L., Allwood A. C., Fischer W. W., Grotzinger J. P., Summons R. E. and
816 Eiler J. M. (2012) Sulfur isotopes of organic matter preserved in 3.45-billion-year-old
817 stromatolites reveal microbial metabolism. *Proc. Natl. Acad. Sci.* **109**, 15146–15151.
- 818 Boussafir M., Gelin F., Lallier-Vergès E., Derenne S., Bertrand P. and Largeau C. (1995) Electron
819 microscopy and pyrolysis of kerogens from the Kimmeridge Clay Formation, UK: Source
820 organisms, preservation processes, and origin of microcycles. *Geochim. Cosmochim. Acta* **59**,
821 3731–3747.
- 822 Bradley A. S., Leavitt W. D., Schmidt M., Knoll A. H., Girguis P. R. and Johnston D. T. (2016) Patterns
823 of sulfur isotope fractionation during microbial sulfate reduction. *Geobiology* **14**, 91–101.
- 824 Brantley S. L., Holleran M. E., Jin L. and Bazilevskaya E. (2013) Probing deep weathering in the Shale
825 Hills Critical Zone Observatory, Pennsylvania (USA): the hypothesis of nested chemical reaction
826 fronts in the subsurface: Nested Reaction Fronts. *Earth Surf. Process. Landf.* **38**, 1280–1298.
- 827 Cai C., Lyons T. W., Sun P., Liu D., Wang D., Tino C. J., Luo G., Peng Y. and Jiang L. (2022) Enigmatic
828 super-heavy pyrite formation: Novel mechanistic insights from the aftermath of the Sturtian
829 Snowball Earth. *Geochim. Cosmochim. Acta* **334**, 65–82.
- 830 Canfield D. E. (1994) Factors influencing organic carbon preservation in marine sediments. *Chem. Geol.*
831 **114**, 315–329.
- 832 Canfield D. E. (1989) Reactive iron in marine sediments. *Geochim. Cosmochim. Acta* **53**, 619–632.
- 833 Canfield Donald E., Farquhar J. and Zerkle A. L. (2010) High isotope fractionations during sulfate
834 reduction in a low-sulfate euxinic ocean analog. *Geology* **38**, 415–418.
- 835 Canfield D. E., Raiswell R., Westrich J. T., Reaves C. M. and Berner R. A. (1986) The use of chromium
836 reduction in the analysis of reduced inorganic sulfur in sediments and shales. *Chem. Geol.* **54**,
837 149–155.
- 838 Canfield Don E., Stewart F. J., Thamdrup B., De Brabandere L., Dalsgaard T., Delong E. F., Revsbech N.
839 P. and Ulloa O. (2010) A Cryptic Sulfur Cycle in Oxygen-Minimum-Zone Waters off the
840 Chilean Coast. *Science* **330**, 1375–1378.
- 841 Chambers L. A., Trudinger P. A., Smith J. W. and Burns M. S. (1975) Fractionation of sulfur isotopes by
842 continuous cultures of *Desulfovibrio desulfuricans*. *Can. J. Microbiol.* **21**, 1602–1607.
- 843 Chandra A. P. and Gerson A. R. (2010) The mechanisms of pyrite oxidation and leaching: A fundamental
844 perspective. *Surf. Sci. Rep.* **65**, 293–315.

- 845 Chen C.-T. A., Lin C.-M., Huang B.-T. and Chang L.-F. (1996) Stoichiometry of carbon, hydrogen,
846 nitrogen, sulfur and oxygen in the particulate matter of the western North Pacific marginal seas.
847 *Mar. Chem.* **54**, 179–190.
- 848 Cole D. B., Reinhard C. T., Wang X., Gueguen B., Halverson G. P., Gibson T., Hodgskiss M. S. W.,
849 McKenzie N. R., Lyons T. W. and Planavsky N. J. (2016) A shale-hosted Cr isotope record of
850 low atmospheric oxygen during the Proterozoic. *Geology* **44**, 555–558.
- 851 Crockford P. W., Hayles J. A., Bao H., Planavsky N. J., Bekker A., Fralick P. W., Halverson G. P., Bui T.
852 H., Peng Y. and Wing B. A. (2018) Triple oxygen isotope evidence for limited mid-Proterozoic
853 primary productivity. *Nature* **559**, 613–616.
- 854 Crockford P. W., Kunzmann M., Bekker A., Hayles J., Bao H., Halverson G. P., Peng Y., Bui T. H., Cox
855 G. M., Gibson T. M., Wörendle S., Rainbird R., Lepland A., Swanson-Hysell N. L., Master S.,
856 Sreenivas B., Kuznetsov A., Krupenik V. and Wing B. A. (2019) Claypool continued: Extending
857 the isotopic record of sedimentary sulfate. *Chem. Geol.* **513**, 200–225.
- 858 Dale A. W., Brüchert V., Alperin M. and Regnier P. (2009) An integrated sulfur isotope model for
859 Namibian shelf sediments. *Geochim. Cosmochim. Acta* **73**, 1924–1944.
- 860 Derry L. A. (2015) Causes and consequences of mid-Proterozoic anoxia. *Geophys. Res. Lett.* **42**, 8538–
861 8546.
- 862 Diamond C. W. and Lyons T. W. (2018) Mid-Proterozoic redox evolution and the possibility of transient
863 oxygenation events eds. T. W. Lyons, M. L. Droser, K. V. Lau, and S. M. Porter. *Emerg. Top.*
864 *Life Sci.* **2**, 235–245.
- 865 Duda J.-P., König H., Reinhardt M., Shuvalova J. and Parkhaev P. (2021) Molecular fossils within
866 bitumens and kerogens from the ~ 1 Ga Lakhanda Lagerstätte (Siberia, Russia) and their
867 significance for understanding early eukaryote evolution. *PalZ* **95**, 577–592.
- 868 Eglinton T. I., Irvine J. E., Vairavamurthy A., Zhou W. and Manowitz B. (1994) Formation and
869 diagenesis of macromolecular organic sulfur in Peru margin sediments. *Org. Geochem.* **22**, 781–
870 799.
- 871 Engel A., Thoms S., Riebesell U., Rochelle-Newall E. and Zondervan I. (2004) Polysaccharide
872 aggregation as a potential sink of marine dissolved organic carbon. *Nature* **428**, 929–932.
- 873 Fakraee M., Hancisse O., Canfield D. E., Crowe S. A. and Katsev S. (2019) Proterozoic seawater sulfate
874 scarcity and the evolution of ocean–atmosphere chemistry. *Nat. Geosci.* **12**, 375–380.
- 875 Fike D. A., Bradley A. S. and Rose C. V. (2015) Rethinking the Ancient Sulfur Cycle. *Annu. Rev. Earth*
876 *Planet. Sci.* **43**, 593–622.
- 877 Fustic M., Ardakani O., Jiang C., Turner E., Mort A., Sanei H., and others (2017) Preliminary petroleum
878 potential and organic matter characterization of the Mesoproterozoic upper Arctic Bay Formation
879 (black shale) at Shale Valley Central, Northern Baffin Island, Nunavut, Canada. In *Gussow*
880 *Geoscience Conference, Lake Louise, Alta., Oct* pp. 8–11.
- 881 Gelin F., Kok M. D., de Leeuw J. W. and Sinninghe Damsté J. S. (1998) Laboratory sulfurisation of the
882 marine microalga *Nannochloropsis salina*. *Org. Geochem.* **29**, 1837–1848.

- 883 Gibson T. M., Shih P. M., Cumming V. M., Fischer W. W., Crockford P. W., Hodgskiss M. S. W.,
884 Wörndle S., Creaser R. A., Rainbird R. H., Skulski T. M. and Halverson G. P. (2018) Precise age
885 of *Bangiomorpha pubescens* dates the origin of eukaryotic photosynthesis. *Geology* **46**, 135–138.
- 886 Gibson T. M., Wörndle S., Crockford P. W., Bui T. H., Creaser R. A. and Halverson G. P. (2019)
887 Radiogenic isotope chemostratigraphy reveals marine and nonmarine depositional environments
888 in the late Mesoproterozoic Borden Basin, Arctic Canada. *GSA Bull.* **131**, 1965–1978.
- 889 Gorjan P., Veevers J. J. and Walter M. R. (2000) Neoproterozoic sulfur-isotope variation in Australia and
890 global implications. *Precambrian Res.* **100**, 151–179.
- 891 Gu X., Heaney P. J., Reis F. D. A. A. and Brantley S. L. (2020) Deep abiotic weathering of pyrite.
892 *Science* **370**, eabb8092.
- 893 Hahn K. E. and Turner E. C. (2017) Composition and history of giant carbonate seep mounds,
894 Mesoproterozoic Borden Basin, Arctic Canada. *Precambrian Res.* **293**, 150–173.
- 895 Hahn K. E., Turner E. C., Babechuk M. G. and Kamber B. S. (2015) Deep-water seep-related carbonate
896 mounds in a Mesoproterozoic alkaline lake, Borden Basin (Nunavut, Canada). *Precambrian Res.*
897 **271**, 173–197.
- 898 Harrison A. G. and Thode H. G. (1958) Mechanism of the bacterial reduction of sulphate from isotope
899 fractionation studies. *Trans. Faraday Soc.* **54**, 84.
- 900 Hartgers W., Lopez J., Sinninghe Damste J., Reiss C., Maxwell J. R. and Grimalt, J. J. (1997) Sulfur-
901 binding in recent environments: II. Speciation of sulfur and iron and implications for the
902 occurrence of organo-sulfur compounds. *Geochim. Cosmochim. Acta* **61**, 4768–4788.
- 903 Hartnett H. E., Keil R. G., Hedges J. I. and Devol A. H. (1998) Influence of oxygen exposure time on
904 organic carbon preservation in continental margin sediments. *Nature* **391**, 572–575.
- 905 Hedges J. I. and Keil R. G. (1995) Sedimentary organic matter preservation: an assessment and
906 speculative synthesis. *Mar. Chem.* **49**, 81–115.
- 907 Hemingway J. D., Rothman D. H., Grant K. E., Rosengard S. Z., Eglinton T. I., Derry L. A. and Galy V.
908 V. (2019) Mineral protection regulates long-term global preservation of natural organic carbon.
909 *Nature* **570**, 228–231.
- 910 Hodgskiss M. S. W., Sansjofre P., Kunzmann M., Sperling E. A., Cole D. B., Crockford P. W., Gibson T.
911 M. and Halverson G. P. (2020) A high-TOC shale in a low productivity world: The late
912 Mesoproterozoic Arctic Bay Formation, Nunavut. *Earth Planet. Sci. Lett.* **544**, 116384.
- 913 Houghton J., Scarponi D., Capraro L. and Fike D. A. (2022) Impact of sedimentation, climate and sea
914 level on marine sedimentary pyrite sulfur isotopes: Insights from the Valle di Manche section
915 (Lower-Middle Pleistocene, southern Italy). *Palaeogeogr. Palaeoclimatol. Palaeoecol.* **585**,
916 110730.
- 917 Ingall E. D. and Cappellen P. V. (1990) Relation between sedimentation rate and burial of organic
918 phosphorus and organic carbon in marine sediments. *Geochim. Cosmochim. Acta* **54**, 373–386.

- 919 Jin Q. and Bethke C. M. (2005) Predicting the rate of microbial respiration in geochemical environments.
920 *Geochim. Cosmochim. Acta* **69**, 1133–1143.
- 921 Jin X., Wu J., Fang P., Zhang Z., Li M. and Zhong N. (2021) Kinetics and fate of organosulphur
922 compounds during the metagenesis stage of thermal maturation: Hydrous pyrolysis investigations
923 on dibenzothiophene. *Mar. Pet. Geol.* **130**, 105129.
- 924 Johnston D. T. (2005) Multiple sulfur isotope fractionations in biological systems: A case study with
925 sulfate reducers and sulfur disproportionators. *Am. J. Sci.* **305**, 645–660.
- 926 Johnston D. T., Wing B. A., Farquhar J., Kaufman A. J., Strauss H., Lyons T. W., Kah L. C. and Canfield
927 D. E. (2005) Active Microbial Sulfur Disproportionation in the Mesoproterozoic. *Science* **310**,
928 1477–1479.
- 929 Jorgensen B. B. (1979) A theoretical model of the stable sulfur isotope distribution in marine sediments.
930 *Geochim. Cosmochim. Acta* **43**, 363–374.
- 931 Kah L. C., Lyons T. W. and Chesley J. T. (2001) Geochemistry of a 1.2 Ga carbonate-evaporite
932 succession, northern Baffin and Bylot Islands: implications for Mesoproterozoic marine
933 evolution. *Precambrian Res.* **111**, 203–234.
- 934 Kah L. C., Lyons T. W. and Frank T. D. (2004) Low marine sulphate and protracted oxygenation of the
935 Proterozoic biosphere. *Nature* **431**, 834–838.
- 936 Kaplan I. R. and Rittenberg S. C. (1964) Microbiological Fractionation of Sulphur Isotopes. *J. Gen.*
937 *Microbiol.* **34**, 195–212.
- 938 Keil R. G., Neibauer J. A., Biladeau C., van der Elst K. and Devol A. H. (2016) A multiproxy approach to
939 understanding the ‘enhanced’ flux of organic matter through the oxygen-deficient
940 waters of the Arabian Sea. *Biogeosciences* **13**, 2077–2092.
- 941 Kelemen S. R., Sansone M., Walters C. C., Kwiatak P. J. and Bolin T. (2012) Thermal transformations of
942 organic and inorganic sulfur in Type II kerogen quantified by S-XANES. *Geochim. Cosmochim.*
943 *Acta* **83**, 61–78.
- 944 Kennedy M. J., Löhr S. C., Fraser S. A. and Baruch E. T. (2014) Direct evidence for organic carbon
945 preservation as clay-organic nanocomposites in a Devonian black shale; from deposition to
946 diagenesis. *Earth Planet. Sci. Lett.* **388**, 59–70.
- 947 Kipp M. A., Krissansen-Totton J. and Catling D. C. (2021) High Organic Burial Efficiency Is Required to
948 Explain Mass Balance in Earth’s Early Carbon Cycle. *Glob. Biogeochem. Cycles* **35**,
949 2020GB006707.
- 950 Kipp M. A. and Stücken E. E. (2017) Biomass recycling and Earth’s early phosphorus cycle. *Sci. Adv.* **3**,
951 eaao4795.
- 952 Knoll A. H. and Sperling E. A. (2014) Oxygen and animals in Earth history. *Proc. Natl. Acad. Sci.* **111**,
953 3907–3908.

- 954 Kohnen M. E. I., Sinninghe Damsté J. S., Kock-van Dalen A. c. and Jan W. D. L. (1991) Di- or
 955 polysulphide-bound biomarkers in sulphur-rich geomacromolecules as revealed by selective
 956 chemolysis. *Geochim. Cosmochim. Acta* **55**, 1375–1394.
- 957 Kohnen M. E. L., Sinninghe Damsté J. S., Ten Haven H. L., Kock-van Dalen A. C., Schouten S. and De
 958 Leeuw J. W. (1991) Identification and geochemical significance of cyclic di- and trisulphides with
 959 linear and acyclic isoprenoid carbon skeletons in immature sediments. *Geochim. Cosmochim.*
 960 *Acta* **55**, 3685–3695.
- 961 Kok M. D., Rijpstra W. I. C., Robertson L., Volkman J. K. and Sinninghe Damsté J. S. (2000a) Early
 962 steroid sulfurisation in surface sediments of a permanently stratified lake (Ace Lake, Antarctica).
 963 *Geochim. Cosmochim. Acta* **64**, 1425–1436.
- 964 Kok M. D., Schouten S. and Sinninghe Damsté J. S. (2000b) Formation of insoluble, nonhydrolyzable,
 965 sulfur-rich macromolecules via incorporation of inorganic sulfur species into algal carbohydrates.
 966 *Geochim. Cosmochim. Acta* **64**, 2689–2699.
- 967 Kunzmann M., Bui T. H., Crockford P. W., Halverson G. P., Scott C., Lyons T. W. and Wing B. A.
 968 (2017) Bacterial sulfur disproportionation constrains timing of Neoproterozoic oxygenation.
 969 *Geology* **45**, 207–210.
- 970 Laakso T. A. and Schrag D. P. (2019) A small marine biosphere in the Proterozoic. *Geobiology* **17**, 161–
 971 171.
- 972 Leavitt W. D., Halevy I., Bradley A. S. and Johnston D. T. (2013) Influence of sulfate reduction rates on
 973 the Phanerozoic sulfur isotope record. *Proc. Natl. Acad. Sci.* **110**, 11244–11249.
- 974 Li C., Love G. D., Lyons T. W., Fike D. A., Sessions A. L. and Chu X. (2010) A Stratified Redox Model
 975 for the Ediacaran Ocean. *Science* **328**, 80–83.
- 976 Li X., Gilhooly W. P., Zerkle A. L., Lyons T. W., Farquhar J., Werne J. P., Varela R. and Scranton M. I.
 977 (2010) Stable sulfur isotopes in the water column of the Cariaco Basin. *Geochim. Cosmochim.*
 978 *Acta* **74**, 6764–6778.
- 979 Liu J., Antler G., Pellerin A., Izon G., Dohrmann I., Findlay A. J., Røy H., Ono S., Turchyn A. V., Kasten
 980 S. and Jørgensen B. B. (2021) Isotopically “heavy” pyrite in marine sediments due to high
 981 sedimentation rates and non-steady-state deposition. *Geology* **49**, 816–821.
- 982 Logan G. A., Hayes J. M., Hieshima G. B. and Summons R. E. (1995) Terminal Proterozoic
 983 reorganization of biogeochemical cycles. *Nature* **376**, 53–56.
- 984 Long D. G. F. and Turner E. C. (2012) Tectonic, sedimentary and metallogenic re-evaluation of basal
 985 strata in the Mesoproterozoic Bylot basins, Nunavut, Canada: Are unconformity-type uranium
 986 concentrations a realistic expectation? *Precambrian Res.* **214–215**, 192–209.
- 987 Luo G., Ono S., Huang J., Algeo T. J., Li C., Zhou L., Robinson A., Lyons T. W. and Xie S. (2015)
 988 Decline in oceanic sulfate levels during the early Mesoproterozoic. *Precambrian Res.* **258**, 36–47.
- 989 Lyons T. W. (1997) Sulfur isotopic trends and pathways of iron sulfide formation in upper Holocene
 990 sediments of the anoxic Black Sea. *Geochim. Cosmochim. Acta* **61**, 3367–3382.

- 991 Lyons T. W., Diamond C. W., Planavsky N. J., Reinhard C. T. and Li C. (2021) Oxygenation, Life, and
992 the Planetary System during Earth's Middle History: An Overview. *Astrobiology* **21**, 906–923.
- 993 Lyons T. W., Luepke J. J., Schreiber M. E. and Zieg G. A. (2000) Sulfur geochemical constraints on
994 mesoproterozoic restricted marine deposition: lower Belt Supergroup, northwestern United
995 States. *Geochim. Cosmochim. Acta* **64**, 427–437.
- 996 Lyons T. W., Reinhard C. T. and Planavsky N. J. (2014) The rise of oxygen in Earth's early ocean and
997 atmosphere. *Nature* **506**, 307–315.
- 998 Mahoney C., März C., Buckman J., Wagner T. and Blanco-Velandia V.-O. (2019) Pyrite oxidation in
999 shales: Implications for palaeo-redox proxies based on geochemical and SEM-EDX evidence.
1000 *Sediment. Geol.* **389**, 186–199.
- 1001 Matrai P. A. and Eppley R. W. (1989) Particulate organic sulfur in the waters of the Southern California
1002 Bight. *Glob. Biogeochem. Cycles* **3**, 89–103.
- 1003 Michiels C. C., Darchambeau F., Roland F. A. E., Morana C., Llíros M., García-Armisen T., Thamdrup
1004 B., Borges A. V., Canfield D. E., Servais P., Descy J.-P. and Crowe S. A. (2017) Iron-dependent
1005 nitrogen cycling in a ferruginous lake and the nutrient status of Proterozoic oceans. *Nat. Geosci.*
1006 **10**, 217–221.
- 1007 Olcott A. N., Downen M. R., Schiffbauer J. D. and Selden P. A. (2022) The exceptional preservation of
1008 Aix-en-Provence spider fossils could have been facilitated by diatoms. *Commun. Earth Environ.*
1009 **3**, 94.
- 1010 Pasquier V., Fike D. A., Révillon S. and Halevy I. (2022) A global reassessment of the controls on iron
1011 speciation in modern sediments and sedimentary rocks: A dominant role for diagenesis. *Geochim.*
1012 *Cosmochim. Acta* **335**, 211–230.
- 1013 Pasquier V., Sansjofre P., Rabineau M., Revillon S., Houghton J. and Fike D. A. (2017) Pyrite sulfur
1014 isotopes reveal glacial–interglacial environmental changes. *Proc. Natl. Acad. Sci.* **114**, 5941–
1015 5945.
- 1016 Petsch S. T., Berner R. A. and Eglinton T. I. (2000) A field study of the chemical weathering of ancient
1017 sedimentary organic matter. *Org. Geochem.* **31**, 475–487.
- 1018 Planavsky N. J., McGoldrick P., Scott C. T., Li C., Reinhard C. T., Kelly A. E., Chu X., Bekker A., Love
1019 G. D. and Lyons T. W. (2011) Widespread iron-rich conditions in the mid-Proterozoic ocean.
1020 *Nature* **477**, 448–451.
- 1021 Planavsky N. J., Reinhard C. T., Wang X., Thomson D., McGoldrick P., Rainbird R. H., Johnson T.,
1022 Fischer W. W. and Lyons T. W. (2014) Low Mid-Proterozoic atmospheric oxygen levels and the
1023 delayed rise of animals. *Science* **346**, 635–638.
- 1024 Planavsky N. J., Slack J. F., Cannon W. F., O'Connell B., Isson T. T., Asael D., Jackson J. C., Hardisty
1025 D. S., Lyons T. W. and Bekker A. (2018) Evidence for episodic oxygenation in a weakly redox-
1026 buffered deep mid-Proterozoic ocean. *Chem. Geol.* **483**, 581–594.
- 1027 Poulton S. W. and Canfield D. E. (2005) Development of a sequential extraction procedure for iron:
1028 implications for iron partitioning in continentally derived particulates. *Chem. Geol.* **214**, 209–221.

- 1029 Poulton S. W. and Canfield D. E. (2011) Ferruginous Conditions: A Dominant Feature of the Ocean
1030 through Earth's History. *Elements* **7**, 107–112.
- 1031 Pye K. and Miller J. A. (1990) Chemical and biochemical weathering of pyritic mudrocks in a shale
1032 embankment. *Q. J. Eng. Geol.* **23**, 18.
- 1033 Raiswell R., Hardisty D. S., Lyons T. W., Canfield D. E., Owens J. D., Planavsky N. J., Poulton S. W.
1034 and Reinhard C. T. (2018) The iron paleoredox proxies: A guide to the pitfalls, problems and
1035 proper practice. *Am. J. Sci.* **318**, 491–526.
- 1036 Raven M. R., Adkins J. F., Werne J. P., Lyons T. W. and Sessions A. L. (2015) Sulfur isotopic
1037 composition of individual organic compounds from Cariaco Basin sediments. *Org. Geochem.* **80**,
1038 53–59.
- 1039 Raven M. R., Fike D. A., Bradley A. S., Gomes M. L., Owens J. D. and Webb S. A. (2019) Paired
1040 organic matter and pyrite $\delta^{34}\text{S}$ records reveal mechanisms of carbon, sulfur, and iron cycle
1041 disruption during Ocean Anoxic Event 2. *Earth Planet. Sci. Lett.* **512**, 27–38.
- 1042 Raven M. R., Fike D. A., Gomes M. L., Webb S. M., Bradley A. S. and McClelland H.-L. O. (2018)
1043 Organic carbon burial during OAE2 driven by changes in the locus of organic matter
1044 sulfurization. *Nat. Commun.* **9**, 3409.
- 1045 Raven M. R., Keil R. G. and Webb S. M. (2021a) Microbial sulfate reduction and organic sulfur
1046 formation in sinking marine particles. *Science* **371**, 178–181.
- 1047 Raven M. R., Keil R. G. and Webb S. M. (2021b) Rapid, Concurrent Formation of Organic Sulfur and
1048 Iron Sulfides During Experimental Sulfurization of Sinking Marine Particles. *Glob. Biogeochem.*
1049 *Cycles* **35**.
- 1050 Raven M. R., Sessions A. L., Fischer W. W. and Adkins J. F. (2016) Sedimentary pyrite $\delta^{34}\text{S}$ differs
1051 from porewater sulfide in Santa Barbara Basin: Proposed role of organic sulfur. *Geochim.*
1052 *Cosmochim. Acta* **186**, 120–134.
- 1053 Rosenberg Y. O., Kutuzov I. and Amrani A. (2018) Sulfurization as a preservation mechanism for the
1054 $\delta^{13}\text{C}$ of biomarkers. *Org. Geochem.* **125**, 66–69.
- 1055 Rosenberg Y. O., Meshoulam A., Said-Ahmad W., Shawar L., Dror G., Reznik I. J., Feinstein S. and
1056 Amrani A. (2017) Study of thermal maturation processes of sulfur-rich source rock using
1057 compound specific sulfur isotope analysis. *Org. Geochem.* **112**, 59–74.
- 1058 Sarret G., Mongenot T., Connan J., Derenne S., Kasrai M., Michael Bancroft G. and Largeau C. (2002)
1059 Sulfur speciation in kerogens of the Orbagnoux deposit (Upper Kimmeridgian, Jura) by XANES
1060 spectroscopy and pyrolysis. *Org. Geochem.* **33**, 877–895.
- 1061 Scholz F. (2018) Identifying oxygen minimum zone-type biogeochemical cycling in Earth history using
1062 inorganic geochemical proxies. *Earth-Sci. Rev.* **184**, 29–45.
- 1063 Shawar L., Halevy I., Said-Ahmad W., Feinstein S., Boyko V., Kamyshny A. and Amrani A. (2018)
1064 Dynamics of pyrite formation and organic matter sulfurization in organic-rich carbonate
1065 sediments. *Geochim. Cosmochim. Acta* **241**, 219–239.

- 1066 Shawar L., Said-Ahmad W., Ellis G. S. and Amrani A. (2020) Sulfur isotope composition of individual
 1067 compounds in immature organic-rich rocks and possible geochemical implications. *Geochim.*
 1068 *Cosmochim. Acta* **274**, 20–44.
- 1069 Sim M. S., Bosak T. and Ono S. (2011) Large Sulfur Isotope Fractionation Does Not Require
 1070 Disproportionation. *Science* **333**, 74–77.
- 1071 Sinninghe Damste J. S. and De Leeuw J. W. (1990) Analysis, structure and geochemical significance of
 1072 organically-bound sulphur in the geosphere: State of the art and future research. *Org. Geochem.*
 1073 **16**, 1077–1101.
- 1074 Sperling E. A. and Stockey R. G. (2018) The Temporal and Environmental Context of Early Animal
 1075 Evolution: Considering All the Ingredients of an “Explosion.” *Integr. Comp. Biol.* **58**, 605–622.
- 1076 Stolper D. A. and Keller C. B. (2018) A record of deep-ocean dissolved O₂ from the oxidation state of
 1077 iron in submarine basalts. *Nature* **553**, 323–327.
- 1078 Stüeken E. E., Kuznetsov A. B., Vasilyeva I. M., Krupenin M. T. and Bekker A. (2021) Transient deep-
 1079 water oxygenation recorded by rare Mesoproterozoic phosphorites, South Urals. *Precambrian*
 1080 *Res.* **360**, 106242.
- 1081 Suess E. (1973) Interaction of organic compounds with calcium carbonate-II. Organo-carbonate
 1082 association in Recent sediments. *Geochim. Cosmochim. Acta* **37**, 2435–2447.
- 1083 Tingle K. E., Porter S. M., Raven M. R., Czaja A. D., Webb S. M. and Bloeser B. (2023) Organic
 1084 preservation of vase-shaped microfossils from the late Tonian Chuar Group, Grand Canyon,
 1085 Arizona, USA. *Geobiology*, gbi.12544.
- 1086 Trust B. A. and Fry B. (1992) Stable sulphur isotopes in plants: a review. *Plant Cell Environ.* **15**, 1105–
 1087 1110.
- 1088 Turner E. C. and Kamber B. S. (2012) Arctic Bay Formation, Borden Basin, Nunavut (Canada): Basin
 1089 evolution, black shale, and dissolved metal systematics in the Mesoproterozoic ocean.
 1090 *Precambrian Res.* **208–211**, 1–18.
- 1091 Turner J. T. (2015) Zooplankton fecal pellets, marine snow, phytodetritus and the ocean’s biological
 1092 pump. *Prog. Oceanogr.* **130**, 205–248.
- 1093 Vairavamurthy A. (1998) Using X-ray absorption to probe sulfur oxidation states in complex molecules.
 1094 *Spectrochim. Acta. A. Mol. Biomol. Spectrosc.* **54**, 2009–2017.
- 1095 Vairavamurthy M. A., Schoonen M. A. A., Eglinton T. I., Luther G. W. and Manowitz B. eds. (1995)
 1096 *Geochemical Transformations of Sedimentary Sulfur.*, American Chemical Society, Washington,
 1097 DC.
- 1098 Van Kaam-Peters H. M. E., Schouten S., Köster J. and Sinninghe Damstè J. S. (1998) Controls on the
 1099 molecular and carbon isotopic composition of organic matter deposited in a Kimmeridgian
 1100 euxinic shelf sea: evidence for preservation of carbohydrates through sulfurisation. *Geochim.*
 1101 *Cosmochim. Acta* **62**, 3259–3283.

- 1102 Van Mooy B. A. S., Keil R. G. and Devol A. H. (2002) Impact of suboxia on sinking particulate organic
1103 carbon: Enhanced carbon flux and preferential degradation of amino acids via denitrification.
1104 *Geochim. Cosmochim. Acta* **66**, 457–465.
- 1105 van de Velde S. J., Reinhard C. T., Ridgwell A. and Meysman F. J. R. (2020) Bistability in the redox
1106 chemistry of sediments and oceans. *Proc. Natl. Acad. Sci.* **117**, 33043–33050.
- 1107 Webb S. M. (2005) SIXPack a Graphical User Interface for XAS Analysis Using IFEFFIT. *Phys. Scr.*,
1108 1011.
- 1109 Werne J. P., Lyons T. W., Hollander D. J., Formolo M. J. and Sinninghe Damsté J. S. (2003) Reduced
1110 sulfur in euxinic sediments of the Cariaco Basin: sulfur isotope constraints on organic sulfur
1111 formation. *Chem. Geol.* **195**, 159–179.
- 1112 Woltz C. R., Porter S. M., Agić H., Dehler C. M., Junium C. K., Riedman L. A., Hodgskiss M. S. W.,
1113 Wörndle S. and Halverson G. P. (2021) Total organic carbon and the preservation of organic-
1114 walled microfossils in Precambrian shale. *Geology* **49**, 556–560.
- 1115 Zaback D. A., Pratt L. M. and Hayes J. M. (1993) Transport and reduction of sulfate and immobilization
1116 of sulfide in marine black shales. *Geology* **21**, 141.
- 1117 Zerkle A. L., Kamyshny A., Kump L. R., Farquhar J., Oduro H. and Arthur M. A. (2010) Sulfur cycling
1118 in a stratified euxinic lake with moderately high sulfate: Constraints from quadruple S isotopes.
1119 *Geochim. Cosmochim. Acta* **74**, 4953–4970.
- 1120 Zhang Z., Li C., Cheng M., Algeo T. J., Jin C., Tang F. and Huang J. (2018) Evidence for Highly
1121 Complex Redox Conditions and Strong Water-Column Stratification in an Early Cambrian
1122 Continental-Margin Sea. *Geochem. Geophys. Geosystems* **19**, 2397–2410.
- 1123 (98 refs)